A Multimodal and Multifunctional CMOS Cellular Interfacing Array for Digital Physiology and Pathology Featuring an Ultra Dense Pixel Array and Reconfigurable Sampling Rate

Author(s):
Wang, Adam Y.; Sheng, Yuguo; Li, Wanlu; Jung, Doohwan; Junek, Greg; Liu, Hangxing; Park, Jongseok; Lee, Dongwon; Wang, Mian; Maharjan, Sushila; Kumashi, Sagar; Hao, Jin; Zhang, Yu S.; Eggan, Kevin; Wang, Hua

Publication date:
2022-12

Permanent link:
https://doi.org/10.3929/ethz-b-000596313

Originally published in:
IEEE Transactions on Biomedical Circuits and Systems 16(6), https://doi.org/10.1109/tbcas.2022.3224064

A Multimodal and Multifunctional CMOS Cellular Interfacing Array for Digital Physiology and Pathology Featuring an Ultra Dense Pixel Array and Reconfigurable Sampling Rate

Adam Y. Wang*†, *Student Member, IEEE*, Yuguo Sheng†, *Student Member, IEEE*, Wanlu Li, Doohwan Jung, *Member, IEEE*, Greg Junek, *Member, IEEE*, Hangxing Liu, *Student Member, IEEE*, Jongseok Park, *Member, IEEE*, Dongwon Lee, *Student Member, IEEE*, Mian Wang, Sushila Maharjan, Sagar Kumashi, *Member, IEEE*, Jin Hao, Yu S. Zhang, Kevin Eggan, and Hua Wang*, *Senior Member, IEEE*

***Abstract*— The article presents a fully integrated multimodal and multifunctional CMOS biosensing/actuating array chip and system for multi-dimensional cellular/tissue characterization. The CMOS chip supports up to 1,568 simultaneous parallel readout channels across 21,952 individually addressable multimodal pixels with 13 µm × 13 µm 2-D pixel pitch along with 1,568 Pt reference electrodes. These features allow the CMOS array chip to perform multimodal physiological measurements on living cell/tissue samples with both high throughput and single-cell resolution. Each pixel supports three sensing and one actuating modalities, each reconfigurable for different functionalities, in the form of full array (FA) or fast scan (FS) voltage recording schemes, bright/dim optical detection, 2-/4-point impedance sensing (ZS), and biphasic current stimulation (BCS) with adjustable stimulation area for single-cell or tissue-level stimulation. Each multi-modal pixel contains an 8.84 µm × 11 µm Pt electrode, 4.16 µm × 7.2 µm photodiode (PD), and in-pixel circuits for PD measurements and pixel selection. The chip is fabricated in a standard 130nm BiCMOS process as a proof of concept. The on-chip electrodes are constructed by unique design and in-house post-CMOS fabrication processes, including a critical Al shorting of all pixels during fabrication and Al etching after fabrication that ensures a high-yield planar electrode array on CMOS with high biocompatibility and long-term measurement reliability. For demonstration, extensive biological testing is performed with human and mouse progenitor cells, in which multidimensional biophysiological data are acquired for comprehensive cellular characterization.**

***Index Terms*— Biosensor, cell-based assay, cellular recording, COVID-19, digital pathology, digital physiology, high resolution, high throughput, impedance sensing, microelectrode array (MEA), multifunctionality, multimodality, optical detection, pandemic, parallel recording, stimulation, switch matrix (SM).**

I. Introduction

With pandemic monitoring and control becoming of paramount importance in public health, the technology need for digital physiology and pathology, which is a collection of high-resolution cellular/tissue-level images uploaded to the cloud for remote analytics and diagnostics [1-3], has rapidly increased to overcome the limitations of in-person lab services, such as processing throughputs and increased exposure risks to patients/medical professionals [4-6]. Currently, cellular physiology diagnoses rely on high-resolution medical imaging [7], and when translated to the cellular or tissue level, these images, even with distinct biomarkers, may not holistically define the prognosis of specific pathogen infections due to the cell's complicated multi-physiological responses [8, 9]. New pathogen or virus varieties, in particular, frequently demonstrate unknown adverse impacts on cellular physiological functions. Recently, various biological, biomedical, healthcare, and pathology applications such as physiological parameterization, drug discovery, COVID-19 detection, and pathophysiological analysis have resorted to CMOS-integrated biosensor arrays over traditional

This work was supported in part by the U.S. Office of Naval Research under grants N00014-16-1-2534 and N00014-17-1-2457 as well as National Science Foundation under Grants 1454555, 1610677, and 2027195. †Adam Wang and Yuguo Sheng are co-first authors. *Corresponding authors: Adam Wang and Hua Wang

A. Y. Wang is with the School of Electrical and Computer Engineering, Georgia Institute of Technology, Atlanta, GA 30332 USA (e-mail: adam.y.wang@gatech.edu).

Y. Sheng, H, Liu, and D. Lee is with the Department of Information Technology and Electrical Engineering, ETH Zurich, 8092 Zurich, Switzerland (e-mail: ysheng@ethz.ch; hangxing@ethz.ch; donlee@ethz.ch).

H. Wang was with the School of Electrical and Computer Engineering, Georgia Institute of Technology, Atlanta, GA 30332 USA. He is now with the Department of Information Technology and Electrical Engineering, ETH Zurich, 8092 Zurich, Switzerland (e-mail: huawang@ethz.ch).

D. Jung, G. Junek, J. Park, and S. Kumashi were with the School of Electrical and Computer Engineering, Georgia Institute of Technology, Atlanta, GA 30332 USA (e-mail: jddoohwan@gmail.com; gregjunek@live.com; ysjspark86@gmail.com; sagar.kumashi@gmail.com).

W. Li and M. Wang were with the Division of Engineering in Medicine, Department of Medicine, Brigham and Women's Hospital, Harvard Medical School, Cambridge, MA, USA 02139 USA (e-mail: wli46@bwh.harvard.edu; mwang37@bwh.harvard.edu).

S. Maharjan and Y. S. Zhang are with the Division of Engineering in Medicine, Department of Medicine, Brigham and Women's Hospital, Harvard Medical School, Cambridge, MA, USA 02139 USA (e-mail: smaharjan@bwh.harvard.edu; yszhang@research.bwh.harvard.edu).

J. Hao and K. Eggan are with the Department of Stem Cell and Regenerative Biology, Harvard Stem Cell Institute, Harvard University, Cambridge, MA 02138, USA (e-mail: jin_hao@g.harvard.edu; eggan@mcb.harvard.edu)

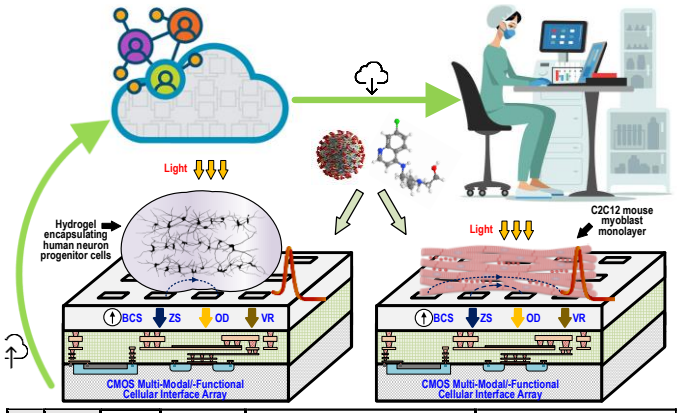

	Modality	Type	Functionalities	Physiological Measurement	Circuit Implementation
↓	VR	Sensing	Full Array Fast Scan	Action potential, local field potential	Voltage amplifiers
↓	OD	Sensing	Dim Light Bright Light	Cell/tissue location, transparency, morphology	Photodiode + source follower
↓	ZS	Sensing	2-Point 4-Point	Cell/tissue-to-surface adhesion, cell proliferation/migration, biofilm formation	Voltage excitation, differential voltage amplifiers, current sensing
↑	BCS	Actuation	Single-Cell Tissue-Level	Cellular networks, cell pacemaking	Current excitation with charge balancing

Fig. 1. Concept of the multimodal/multifunctional CMOS cellular interface array for digital pathology/physiology.

microelectrode arrays (MEAs) for massive parallelism and enhanced throughput in diagnostics [10-31]. In particular, the virtual acquisition, management, interpretation, and diagnosis from digital physiology and pathology can be significantly facilitated using CMOS-integrated biosensor arrays, providing a paradigm shift in these disciplines. Although current CMOS cell-based biosensors provide a wide range of sensing capabilities, most of them each specialize in a single modality such as CMOS-based MEAs, where only electrophysiological data can be recorded [24, 32-38]. As a result, such platforms are only capable of monitoring one sort of biophysiological response and are incapable of capturing the cell's highly complicated and frequently unknown physiological responses [39, 40]. Though some sensor/actuator designs claim to be multi-functional, some of their modalities still rely on the same signal transduction mechanisms, such as wideband or narrow-band biopotential monitoring or stimulation in electrical voltages/currents, and they are hence single-modality in nature [41-44].

CMOS-based biosensor arrays with in-pixel multimodal sensing for holistic cellular/tissue characterization were proposed and demonstrated in 2015 [8]. The monitoring of various parameters such as cellular potential, impedance, and optical responses in real time was achieved in each individually configured and controlled pixel, enabling a sensor array to monitor multiple cellular physiological properties at the single pixel level, radically extending our abilities to study digital physiology and pathology of cells and tissues. However, despite various previously reported multimodal CMOS biosensor arrays [8, 9, 14, 16, 17, 43-52] and considering their higher complexity compared to single-modal biosensors, there is still a great need to significantly advance multimodal CMOS biosensors arrays with higher pixel density, higher sampling rate, improved area efficiency, higher yield during post-CMOS processing, optimized electrodes for biological interfacing, and new reconfigurable sensing/actuation modalities. These desired features will enable next-generation digital physiology/pathology cellular characterization platforms to extract a vast assortment of different physiological information from various cells under various settings, including those with fast physiological characteristics, such as neuron/cardiac cells.

To address these challenges, this paper presents an extension of our CMOS cellular sensing and actuating array [45], conceptually shown in Fig. 1, with 21,952 individually addressable multimodal pixels with a 13-µm center-to-center pixel pitch fully integrated into a 2.91 mm × 1.28 mm active sensing area, achieving both single-cell resolution and tissue-level field-of-view (FoV). Each pixel supports four multifunctional modalities, including three multi-modal sensing modalities, (1) full array (FA) or fast scan (FS) voltage recording (VR) to investigate cellular electrical activity and ion concentration [17, 42, 43], (2) bright/dim optical detection (OD) to examine cell morphology and transparency [51, 53], and (3) 2-/4-point impedance sensing (ZS) imaging to track cell adhesion and contractility [14, 43, 47, 54-56], as well as a cellular actuating modality in the form of single-cell/tissue-level biphasic current stimulation (BCS) to achieve cell electrical stimulation, controlled charge delivery, and membrane electroporation [17, 57]. Each modality can be reconfigured for different functionalities with adjustable scan rates versus FOV in VR to operate as FA, which analyzes the whole active area, or FS, which enables the recording of sharp electrophysiological changes, variable reset periods in OD to accommodate bright or dim lighting, programmable selection of pixels in ZS to permit 2- or 4-point ZS, and configurable stimulation area in BCS to excite selective single cells in a culture or collectively a tissue sample. To our knowledge, this reported architecture provides the most multifunctional modalities for cellular interfacing, highest pixel density, and smallest pixel pitch size for high-resolution recording and imaging among reported CMOS multi-modality cellular arrays with OD. The device can support up to 1,568 simultaneous parallel recording channels enabling high throughput recording. With the combination of the reconfigurable scan rate of up to an extremely fast 45.8 kS/s, state-of-the-art ultra-high density multifunctional multimodal pixel array of 5893 pixels/mm^2, and an extremely biocompatible and chemically stable electrode array from our novel design and high-yield in-house post-CMOS fabrication process which achieves 100% electrode deposition coverage over the pixel array without peel off, our platform can readily extract different cellular physiological features with rapid features with minimal cell death for long periods (> 1 month) and uniquely advance holistic cellular and tissue characterizations. With the combination of an ultra-fast scan rate of up to 45.8 kS/s and small pixel size of 13 × 13 µm^2, our cellular interfacing array seeks to eventually accurately capture and sort neural spikes with high signal-to-noise ratio (SNR) to provide a high-resolution mapping of a neural network.

This article is organized as follows. Section II explains the architecture and main circuit blocks of the demonstrated multimodal and multifunctional CMOS cellular interfacing chip. Section III details the novel in-house post-CMOS processing, packaging, and experimental measurement setup of the chip. Section IV presents the measurement results through electrical and extensive *in vitro* biological experiments with human and mouse progenitor cell cultures. Finally, Section V concludes this article.

This article has been accepted for publication in IEEE Transactions on Biomedical Circuits and Systems. This is the author's version which has not been fully edited and content may change prior to final publication. Citation information: DOI 10.1109/TBCAS.2022.3224064

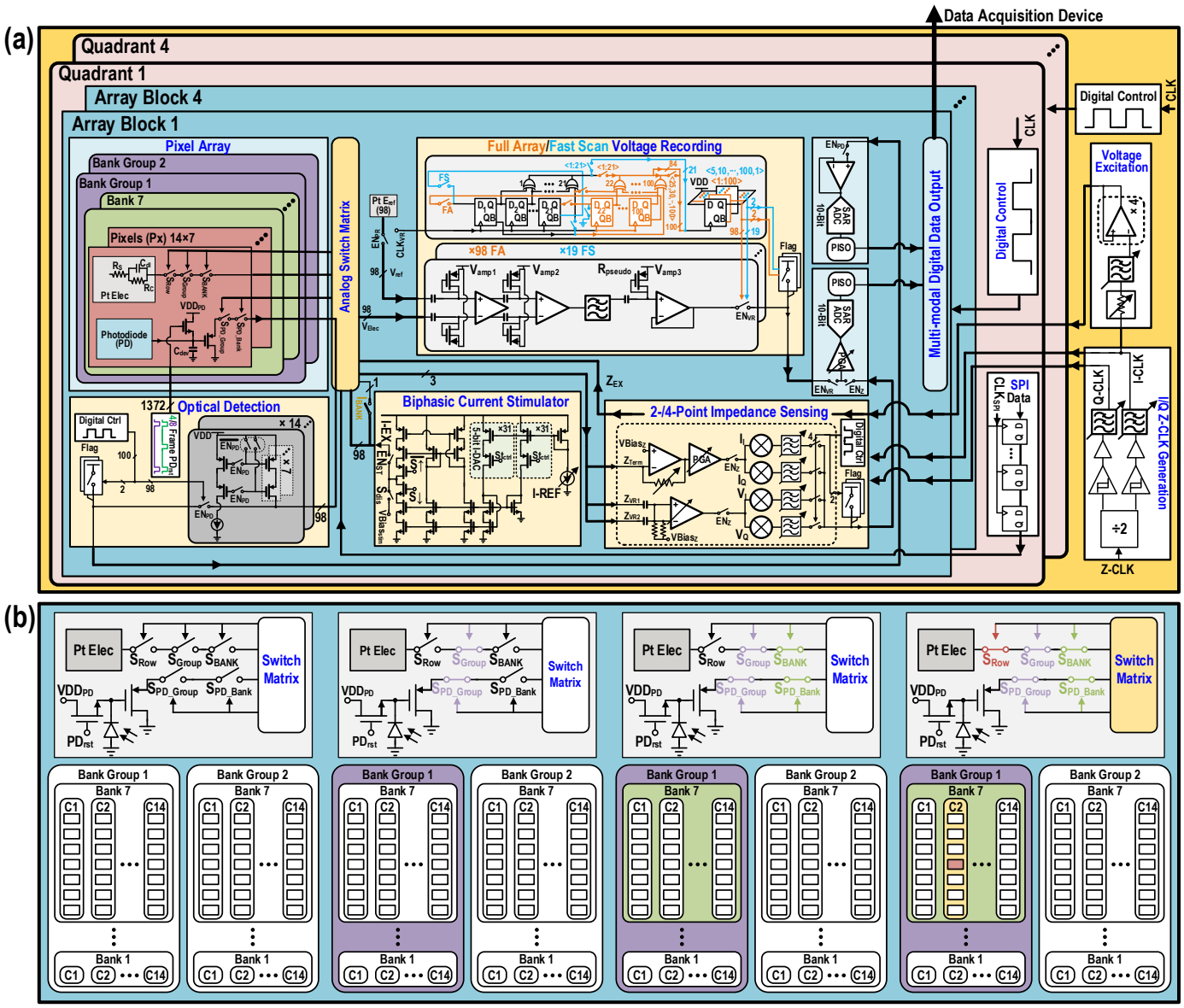

Fig. 2. (a) High-level system architecture of the integrated multi-modal/-functional CMOS sensing/actuating array. (b) Example of pixel selection process using the in-pixel circuitry. The highlighted green, violet, yellow, and red shadings represent the selected bank group, bank, bank column, and pixel row, respectively.

II. CMOS Multi-Modal Multi-Functional Cellular Sensing/Actuating Array

The system architecture of the demonstrated CMOS multi-modal cellular interfacing array is depicted in Fig. 2a. The chip contains 16 multi-modal/-functional array blocks divided into four quadrants, digital serial peripheral interface (SPI) circuits to program the various circuit modules and functionalities on-chip, and a clock generation module which provides the voltage excitation for complex ZS. Each array block contains circuits for all modalities/functionalities, switch matrix (SM), SPI controls, and readout with two 10-bit successive approximation (SAR) analog-to-digital converters (ADCs), with one ADC streaming out VR or ZS while the other ADC outputs OD data. Each array block contains 98 Pt reference electrodes (E_{ref}) for VR and features 1,372 pixels divided into 14 pixel banks (98 pixels/bank) split between two bank groups (7 banks/group). Hence, with 16 array blocks × 2 groups/array block × 7 banks/group and 98 pixels/bank, the chip achieves a total of 21,952 13 µm × 13 µm pixels, which were compactly laid out within a 2.91 mm × 1.28 mm area, realizing an electrode density of 5893 pixels/mm^2, enabling both single-cell resolution and tissue-level field-of-view (FoV). The resulting 2.91 mm × 1.28 mm sensing area reserves enough area for the analog front-end (AFE) and readout circuitries within the 7 mm × 7 mm chip area. Each pixel is comprised of one 8.84 µm × 11 µm Pt electrode, one 4.16 µm × 7.2 µm reverse-biased p+/n-well/p-sub photodiode (PD), circuits for PD measurements, and switches for the pixel selection. The pixel is laid out in a compact 13 µm × 13 µm footprint, the smallest reported multimodal sensing pixel containing a PD, while also comparable to or smaller than the sizes of previously reported single-modal pixels [58-61]. Fig. 2b details the pixel selection controlled by the SM. For OD, the S_{PD_Group} switch selects the bank group within an array block while S_{PD_Bank} specifies the bank within the group. Similarly, for all other modalities, S_{Group} and S_{Bank} determine which group and specific bank, respectively. For ZS and current stimulation modalities, the

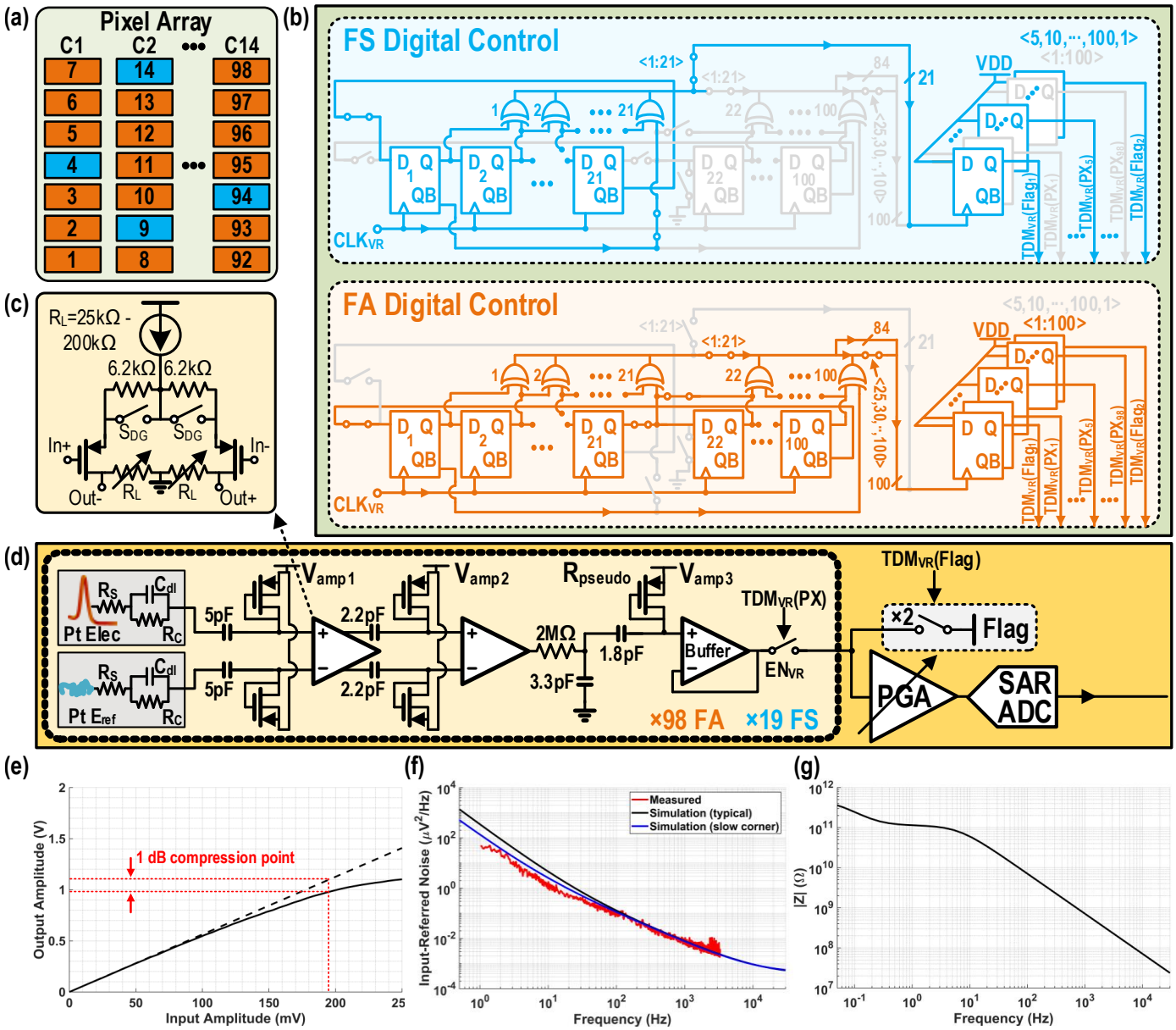

Fig. 3. FA and FS VR modality. (a) Pixel layout in a pixel bank with blue pixels representing FS pixels. (b) FA (orange) and FS (blue) digital control schematics. (c) First stage amplifier schematic used in VR. (d) VR modality circuit module. Simulation of VR AFE (e) linearity, (f) input-referred voltage noise with measurement comparison, and (g) input impedance.

switch matrix selects a specific column in the bank determined by S_{Bank} and the switch S_{Row} configures the pixel within the column. Each of the 7 pixels within a column has a S_{Row} controlled by a unique control signal. During VR, the S_{Row} is closed for all pixels across the bank's 14 columns. Therefore, by programming the array block/in-pixel SM, all pixels can be configured for any modality/functionality. For each modality/functionality, the switches to select the pixel group, bank, and row are preconfigured before recording to prevent the introduction of folding noise.

A. Full Array (FA) and Fast Scan (FS) Voltage Recording

To properly record subtle feature changes in fast physiological inputs, such as neuron action potentials (APs), the VR modality detailed in Fig. 3 inside each array block is adjustable for multiple sampling speeds and scan functionalities. During the VR modality, the in-pixel switches (S_{Group}/S_{Bank}/S_{Row}) are enabled to choose one bank in an array block while the OD switches (S_{PD_Group}/S_{PD_Bank}) are disabled. In the VR modality, switches operated by the digitally controlled time-division multiplexing (TDM) signals, shown in Fig. 3b, operate in either a Full Array (FA) or Fast Scan (FS) functionality. The FA functionality scans through each full pixel bank at a high pixel array resolution with 1,568 concurrent pixel readouts across 16 parallel array blocks. In contrast, the FS functionality samples every fifth pixel, as depicted in the color-coded pixel array in Fig. 3a, to achieve an increased sampling rate of 4.76 times at a lower pixel array resolution with 304 concurrent pixel readouts. The timing diagrams for the digital control of the FA and FS VR are illustrated in Fig. 4. The VR module shown in Fig. 3b-d consists of a 3-stage programmable differential amplifier chain that amplifies the detected differential biopotential signals between a Pt sensing electrode and Pt E_{ref}. Each VR module has its own unique Pt E_{ref} to accommodate a corresponding pixel in a bank,

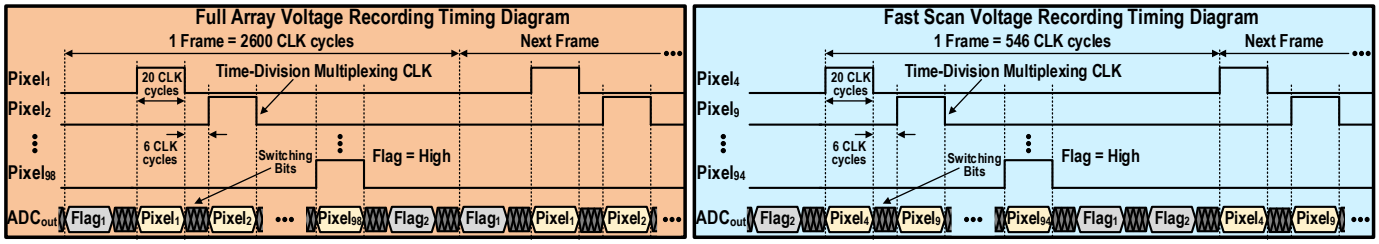

Fig. 4. TDM timing diagram for FA and FS VR modality.

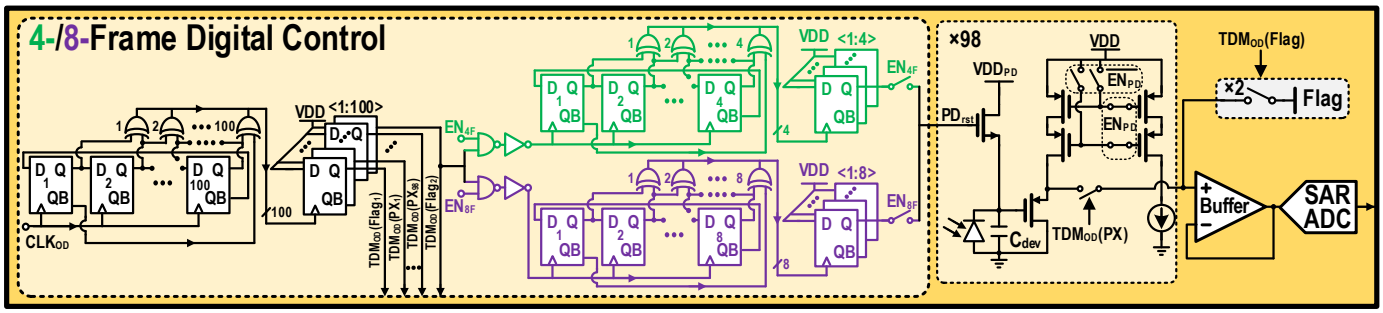

Fig. 5. Circuit module OD with its digital control schematics for bright (green) and dim (purple) functionalities.

preventing crosstalk over the 98 VR modules in an array block. In addition, only one bank per array block is active during VR, so the 98 reference electrodes are shared amongst the 14 banks within an array block. At the input of each amplifier stage, DC-biasing pseudo-resistors and AC coupling capacitors serve as a high-pass filter (HPF) with a 0.2 Hz cutoff. The second stage amplifier shares the same topology as the first stage amplifier in Fig. 3c. Although using one of the differential outputs of the second stage reduces the maximum realized gain by 6 dB, the loss of a 6 dB of gain is not significant since the 3-stage amplifier chain generated a gain of up to 70 dB, which is sufficient for cellular electrophysiology recording. At the output of the second amplifier, a low pass filter (LPF) with a cutoff of 22.5 kHz is implemented to eliminate high-frequency noise. The recording 0.7 Hz – 22.5 kHz bandwidth is adequate to collect the local field potential (LFP) and AP from neurons. Furthermore, each amplifier can be optionally employed with source degeneration, using the switch S_{DG} controlled by the SPI, to desensitize photo-resistive DC offsets brought on by leakage current and mismatches between input transistors and 3-bit tunable load resistors R_L. Each array block contains 98 VR modules with each module corresponding to one of the 98 pixels from a pixel bank. The corresponding pixels from each of the 14 pixel banks share the same VR module. As the third amplifier stage, a voltage buffer is implemented to drive the subsequent programmable gain amplifier (PGA) input, which is shared by 98 VR modules through TDM, allowing quick tracking of the amplified signals. The AFE has a simulated 1 dB compression point at an input voltage amplitude of 195 mV, measured integrated noise of 10.5 μV_{rms} and 4.35 μV_{rms} in LFP and AP bands, respectively, and high input-impedance as demonstrated in Fig. 3e-f, which is more than sufficient to faithfully amplify and capture biological signals such as neural action potentials. In addition, the simulated CMRR and PSRR of the AFE are 65.4 and 51.3 dB, respectively. In the FS functionality, 19 of the 98 FA VR modules are chosen by the TDM to be selected as the 19 FS pixels that the ADC will read out. The VR module is linked to TDM switches and two data

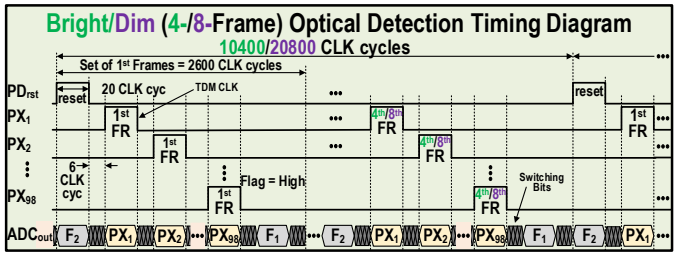

Fig. 6. TDM timing diagram for bright/dim OD.

reference flags, followed by a PGA sampled at 961.5 kHz by a 10-bit SAR ADC, yielding sampling speeds in the FA and FS functionalities of 9.62 kHz/pixel over 98 pixels in a bank, totaling 1,568 parallel pixel readouts over 16 array blocks and 45.8 kHz/pixel for 19 pixels/bank, resulting in 304 concurrent pixels across the 16 array blocks, respectively. The sampling rate provided by the FS functionality is essential for precisely capturing, sorting, and reconstructing acute neuronal APs and local field potentials [62, 63]. The ultra-fast scan rate from the FS functionality enables high SNR recording while the small pixel size of 13 × 13 μm^2 provides high-resolution cellular electrical network mapping when utilizing the FA functionality. The gain of the whole VR modality can be tuned from 15 – 70 dB, allowing the VR dynamic range to be adjusted to accommodate varying cell positioning and activity levels.

B. Bright or Dim Light Optical Detection

The OD modality captures the optical shadow imaging of cells to observe cell positioning, morphology, and transparency variations, which eliminates the need for large and costly conventional optical setups in cell imaging [51, 53]. During the OD modality, the in-pixel switches (S_{PD_Group}/S_{PD_Bank}) are switched on to choose one bank in an array block while the other modality switches (S_{Group}/S_{Bank}/S_{Row}) are turned off. The TDM signals and switching can be programmed, as shown in Fig. 5 with its timing diagram drawn in Fig. 6, to operate in either a bright or dim functionality, which resets the PD_{rst} signal with TDM every 4 or 8 frames, respectively, with each frame

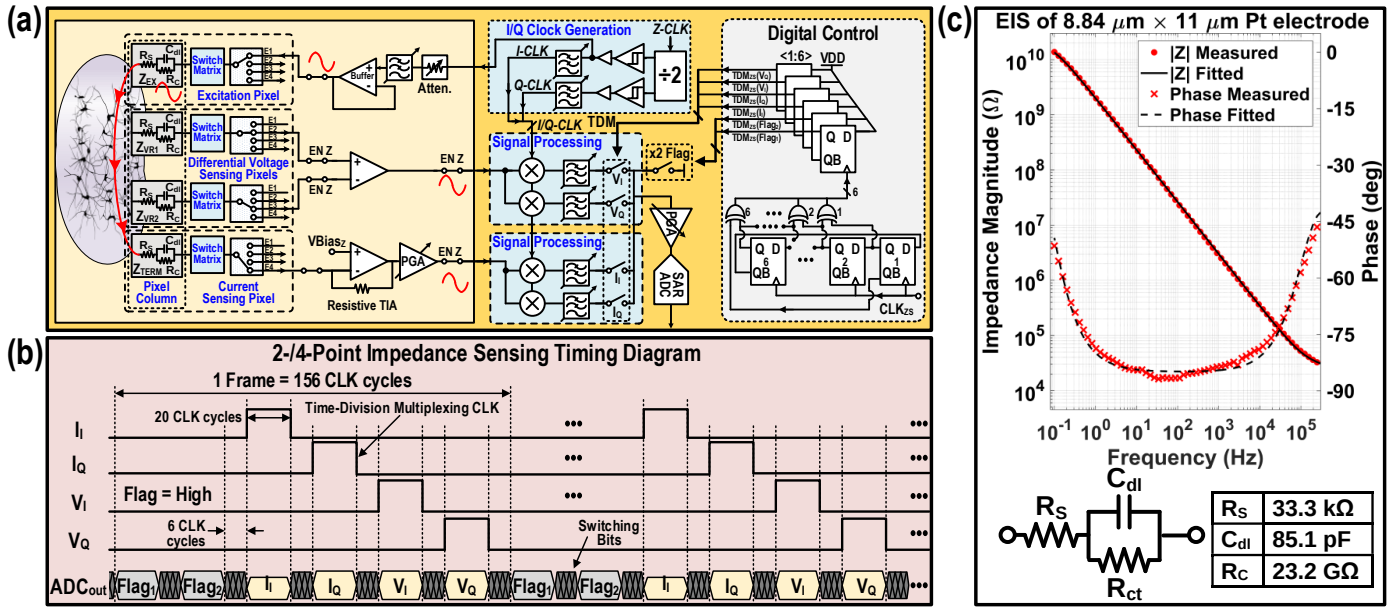

Fig. 7. (a) Circuit module for the 2-/4-point ZS modality and its digital control. (b) TDM timing diagram for ZS. (c) Measured electrochemical impedance spectroscopy overlayed with fitted values using extracted electrode-electrolyte impedance model of the pixel's microelectrode.

representing 2,600 clock cycles. The OD module in Fig. 5 consists of a reverse-biased p+/n-well/p-substrate PD with a PD reset nMOS transistor switch with the drain and source connected to VDD_{PD} and a source-follower amplifier, respectively, cascaded pMOS transistors with switches to enable (EN_{PD} high) or disable ($\overline{EN_{PD}}$ high) OD, and TDM signals/switches. The nMOS transistor switch is activated during the reset period where the PD_{rst} node becomes high, charging the cathode of the PD to VDD_{PD} (1.2 V) during 20 clock cycles. The nMOS switches are disabled after the reset time, and the parasitic device capacitors at the gate of the pMOS source follower are discharged by the photocurrent produced in the PD over 10380 or 20780 clock cycles under the bright or dim functionality, respectively. Each array block contains 98 OD modules with each module corresponding to one of the 98 pixels from a pixel bank. The corresponding pixels from each of the 14 pixel banks share the same OD module. The 98 OD modules are connected to TDM switches to a buffer sampled at 384 kHz by a 10-bit SAR ADC, yielding sampling speeds of 3.84 kHz/pixel for 1,568 parallel OD pixel outputs across 16 array blocks. With the bright functionality, the chip is exposed to a higher intensity light source in which a better contrast for cellular transparency/morphology can be detected without the PD discharging too fast and saturating because the discharging voltage slope is proportional to optical intensity. With the dim functionality, the chip is exposed to a low intensity light source to prevent phototoxicity and accidental photo-stimulation of cells [64, 65].

C. *Two-Point and Four-Point Complex Impedance Sensing*

The circuit module involved in 2- and 4-point, or -electrode, complex impedance detection is described in Fig. 7a with the timing diagram for the digital control shown in Fig. 7b. The standard 2-point approach detects the electrode-electrolyte/medium interfacial impedance modeled in Fig. 7c from both electrodes in series with the load impedance, in this case, the cell impedance, by dividing the excitation voltage supplied to an excitation pixel over a measured current from a terminal pixel [16, 51]. The 2-point cellular impedance sensing is widely used in CMOS cellular sensor arrays due to their circuit simplicity, low overhead, and high spatial resolution.

However, the 2-point impedance measurements will become problematic when electrodes are scaled down because the electrode-electrolyte interfacial impedance starts to dominate sample impedance, especially at lower frequencies [66-68]. With 4-point impedance, the double layer capacitance (C_{dl}) and charge transfer resistance (R_{ct}) from the electrode-electrolyte impedance presented in Fig. 7c are eliminated since the differential voltage between two adjacent pixels is detected and divided by the measured current. Eliminating the electrode-medium impedance enables accurate surveillance of cell adhesion, proliferation, and membrane impedance over the CMOS cellular interfacing array [14, 47]. The 4-point ZS consists of four pixels: Z_{EX} for in-phase voltage excitation, Z_{VR1} and Z_{VR2} for differential voltage sensing, and Z_{TERM} for current sensing, which can be configured in any orientation within a pixel bank column through a switch matrix. The 2-point ZS omits the two differential voltage sensing pixels VR_1 and VR_2.

To begin the impedance detection, four neighboring pixels in a bank column are picked via in-pixel switches and the switch matrix. During the ZS modality, the in-pixel switches (S_{Group}/S_{Bank}) are enabled to choose one bank in an array block while the OD switches (S_{PD_Group}/S_{PD_Bank}) are disabled. The switch S_{Row} determines the role of a pixel within a 7-pixel column (Z_{EX}/Z_{VR1}/Z_{VR2}/Z_{TERM}/unused). The first electrode Z_{EX} provides a programmable 11.6 – 500 mV amplitude, 15 – 500 kHz voltage excitation signal, $V_{ex} = A\sin(\omega t)$, sourced from an externally provided clock signal, Z-CLK. Z-CLK is delivered into a digital divide-by-2 logic circuit, which creates two clock signals that are 90° phase-shifted with respect to one another. These signals are routed via a 6-bit programmable 4th-order LPF to generate in-phase and quadrature-phase (I/Q) sinusoidal signals which are also fed to the mixers in the signal processing circuits. For voltage excitation, the in-phase

sinusoidal signal passes through a 5-bit attenuator (0 – 42 dB) to decrease its amplitude to avert any undesirable electrochemical reactions through the Pt microelectrode and culture medium. The attenuated signal is utilized for voltage excitation and is transmitted to a voltage buffer, which drives the excitation electrode, Z_{EX}. The current generated by the voltage stimulation flows through the cells and into the fourth electrode, Z_{TERM}, which is connected to a resistive transimpedance amplifier (TIA) with a transimpedance gain tunable from 20 kΩ to 200 kΩ. The TIA detects the complex current signal, performs current-to-voltage conversion, and is amplified by a PGA with a gain from 0.2 to 23 dB. For signal processing, the output is delivered to a differential mixer with a conversion gain of 12 dB, which demodulates the measured signal and extracts its real and imaginary components, followed by a programmable LPF, resulting in the down-converted current sensing signals I_I and I_Q. To calibrate the offsets, the impedance sensing modality is first operated in the absence of an excitation signal to obtain the reference down-converted current sensing signals I_{Iref} and I_{Qref}. Therefore, with Z_{EX} and Z_{TERM} electrodes, the magnitude and phase of the 2-point impedance can be calculated as shown in (1) and (2), respectively.

$$|Z_{2-pt}| = \frac{A}{\sqrt{(I_I - I_{Iref})^2 + (I_Q - I_{Qref})^2}} \quad (1)$$

$$\angle Z_{2-pt} = -\tan^{-1}\left(\frac{I_I - I_{Iref}}{I_Q - I_{Qref}}\right) \quad (2)$$

To obtain the 4-point impedance, a differential voltage sensing amplifier with a gain of 0.2 – 23 dB detects the voltage difference between the second and third electrodes (Z_{VR1} and Z_{VR2}), which is then transformed to complex voltage signals via signal processing through mixers (12 dB) and LPFs. The down-converted signals V_I and V_Q are obtained with the presence of the excitation signal while the reference signals V_{Iref} and V_{Qref} are recorded in the absence of an excitation signal. With all four pixels, the derived magnitude and phase components of the complex 4-point impedance are presented in (3) and (4), respectively.

$$|Z_{4-pt}| = \frac{\sqrt{(V_I - V_{Iref})^2 + (V_Q - V_{Qref})^2}}{\sqrt{(I_I - I_{Iref})^2 + (I_Q - I_{Qref})^2}} \quad (3)$$

$$\angle Z_{4-pt} = \tan^{-1}\left(\frac{V_I - V_{Iref}}{V_Q - V_{Qref}}\right) - \tan^{-1}\left(\frac{I_I - I_{Iref}}{I_Q - I_{Qref}}\right) \quad (4)$$

With 2-point impedance sensing, Z_{EX} and Z_{TERM} can be arranged adjacently so the impedance between two adjacent pixels can be obtained for higher resolution impedance mapping. On the other hand, 4-point impedance removes the high impedance of the C_{dl} and R_{ct} of the subcellular Pt microelectrode, leaving two solution resistances ($2R_s$ = ~ 65 kΩ), a relatively low value, in series with the cell impedance.

D. Single-Cell/Tissue-Level Biphasic Current Stimulation

The biphasic current stimulation (BCS) modality with charge balancing is utilized to excite cellular samples, invoking an electrical response that is useful in applications such as neuromodulation, electroporation, cardiac pacemaker, and cellular network mapping [17, 42, 57, 69]. The BCS modality is equipped with two functionalities: single cell, where any of 1 – 4 pixels per pixel bank is excited (16 – 64 pixels across 16 array blocks), or tissue-level, in which current is delivered to all 98 pixels per bank (1,568 pixels over 16 array blocks). The circuit module per array block and output current involved in BCS is depicted in Fig. 8. During the BCS modality, the in-pixel switches (S_{Group}/S_{Bank}) are activated to choose one bank in an array block while the OD switches (S_{PD_Group}/S_{PD_Bank}) are disabled. When configured for single-cell stimulation, the SM (pathing highlighted cyan in Fig. 8a) determines which bank column will be utilized and the switch S_{Row} determines which 1 – 4 pixels within a 7-pixel bank column will receive BCS. For tissue-level stimulation, the SM (pathing highlighted orange in Fig. 8a) shorts all the bank columns, and the switch S_{Row} is activated for all pixels in the bank column, thereby shorting all 98 pixels in a pixel bank.

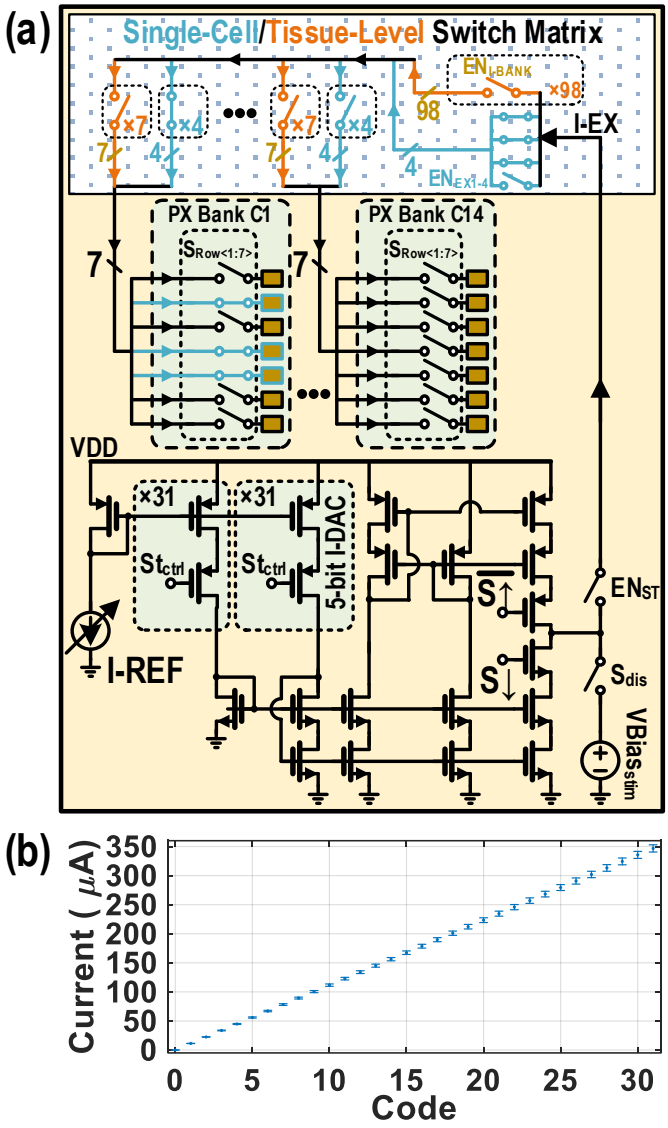

Fig. 8. (a) Circuit module and SM operations for the BCS modality configured for single-cell (cyan) and tissue-level (orange) functionalities. (b) Simulated current output across all codes using Monte Carlo method with 200 samples.

The BCS is provided using 5-bit current digital-to-analog converters for up to 340 µA as shown in Fig. 8b with a reference current generated on-chip. The output current is dependent on the output voltage and is limited by the compliance voltage (3.3 V). To address this issue, when utilizing tissue-level stimulation, the shorting of the 98 pixels lowers the impedance load for stimulation, which prevents the output voltage from reaching compliance so the output current exhibits linearity over input codes as shown in Fig. 8b. For single-cell stimulation, which will have a higher impedance load, only a small amplitude of stimulation current is needed (<15 µA), resulting in the use for only a few input codes, ensuring that the compliance voltage will not be reached by the output. To provide charge balancing, the anodic and cathodic pulses are activated sequentially with the signals $\overline{S\uparrow}$ and $S\downarrow$, respectively. The pulse width and time between pulses can be arbitrarily chosen. After BCS, the excited pixel is connected to $VBias_{stim}$ via the switch S_{dis} to expel any residual charge, preventing electrode corrosion which can harm biological samples. Additionally, the BCS with adjustable stimulation area in each array block can be conjoined simultaneously with the VR modality to observe the electrical activity of the excited cellular samples. In addition, we can simultaneously stimulate the cells with BCS during the middle of running FA or FS VR because the circuit modules are separately controlled by SPI.

III. System Integration

A. *In-House Post-Processing for Multi-Modal CMOS Arrays*

The multi-modal CMOS cellular interfacing array occupies 7 mm × 7 mm in a standard 130 nm BiCMOS process. Since the top metal option used in 130 nm BiCMOS and other standard CMOS processes is Al, the on-chip electrodes of the foundry-fabricated CMOS ICs will need to undergo high-quality surface modifications since exposed Al possesses a native surface oxide, a dielectric, increasing its impedance [70]. In addition, Al will react with the cell culture medium, causing irreversible damage to the electrode while also leaking Al compounds that are toxic to cell cultures [16, 71].

To address this issue, a noble biocompatible metal such as Au or Pt must replace the Al electrode surface native to CMOS processes. A common method previously used by other reported CMOS sensor arrays involves an electroless process called electroless nickel immersion Au which deposits a metal stack of Zn/Ni/Au on top of the Al layer [16, 46-48, 71-74]. However, since the thickness of the Au coating is dependent on the electrode size due to the chemical nature of this process, the processing recipe will need to be iteratively and empirically optimized to ensure full surface Au coverage, especially near the corner, edges, and sidewalls of the electrode. Any exposure of the underlying Al layer will render the chip unsuitable for cell culturing as demonstrated previously [16]. Other CMOS sensor arrays utilize processes that directly deposit and pattern photolithography biocompatible materials over the Al surface using sputtering or electron-beam physical vapor deposition (EBPVD) [41-43, 75]. However, this method will not eliminate the native Al oxide, resulting in a large increase in electrode impedance. In addition, if any deposited surface over the Al is peeled off during the lift-off step due to mechanical agitation, e.g., ultrasonication, the CMOS chip again will be rendered bioincompatible, thus lowering the overall yield.

Since bioincompatibility in CMOS originates from the native Al top metal, we have developed an in-house fabrication process that eliminates all the Al top metal over the pixel array to completely obviate unwanted chemical reactions and toxic Al ion leakage. The chip images and conceptual cross sections throughout the fabrication process are presented in Fig. 9. In the designing of our multi-modal cellular interfacing array, we have connected all pixels and reference electrodes using Al top metal from the foundry. The CMOS chip from the foundry will undergo our CMOS-compatible in-house post-processing methods to enhance their biocompatibility. First, the chips are cleaned via spray rinsing in acetone followed by methanol, isopropanol, and DI water. Then, the wire-bond pads are covered in photoresist and the chip is immersed in Al etchant to completely etch away the Al over the pixel and reference electrode array, exposing the underlying tungsten vias. Afterward, the photoresist over the pads is stripped and a bilayer resist stack is spin-coated onto the chip, patterned, and then developed. Eventually, a Ti/Pt layer is sputter deposited over all the electrodes in the pixel array followed by a lift-off without the need for ultrasonication. Pt was chosen instead of Au due to Pt's lower electrode-electrolyte impedance while possessing similar inertness and stability [66-68]. Our in-house process possesses some key advantages over previously reported methods of eliminating Al and using EBPVD [14, 16].

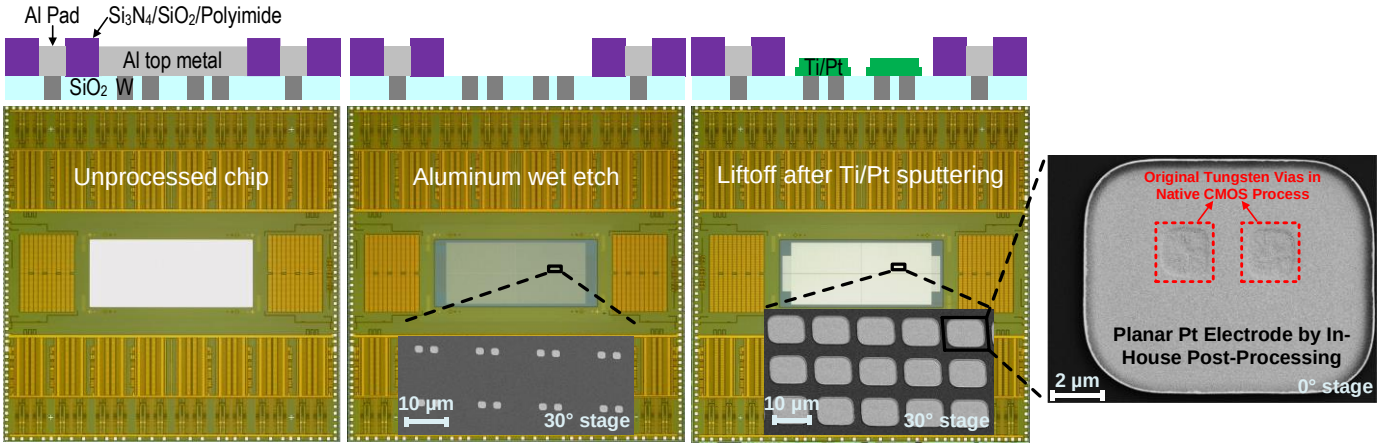

Fig. 9. Conceptual cross sections, chip microphotographs, and scanning electron microscope images of Al shorting all pixels before processing, pixel isolation after Al wet etching, and uniform biocompatible electrode fabrication after Pt deposition.

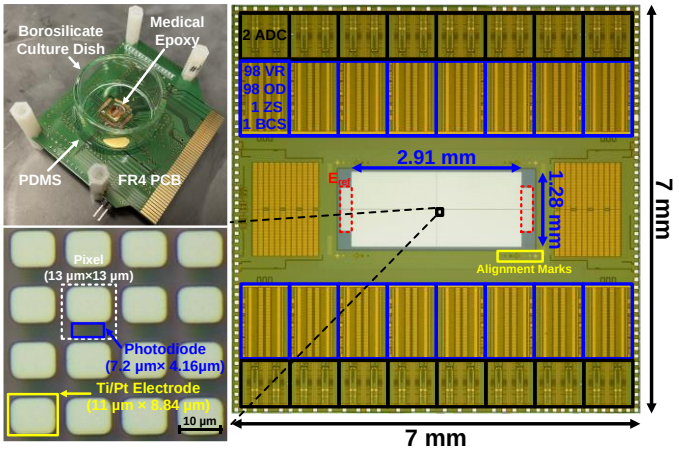

Fig. 10. Fully packaged biocompatible multi-modality sensor array on daughter PCB and die microphotograph with zoomed-in view of pixels with post-processed Pt microelectrodes.

The resulting Al-etched pixel array is completely planarized, enabling the use of a bilayer resist stack to perform sputter deposition without exposure to the high temperature in EBPVD. In addition, we can maximize the electrode size beyond the layout design rules of the CMOS process mandated by the foundry, reducing the overall electrode-electrolyte interfacial impedance and improving signal integrity [66-68].

Our in-house process achieves high yield with 100% successful Pt coating over all 21,952 pixels and 1,568 E_{ref} with no peel-off as demonstrated in Fig. 9 and Fig. 10 and extreme biocompatibility with minimal cell death over a month of culturing as shown in Fig. 11a, enabling long-term cellular recording. The resulting Pt electrodes are shown to be highly chemically stable in the standard PBS buffer solution. Long-term electrochemical impedance spectroscopy (EIS) is performed by an off-the-shelf potentiostat (Biologic VMP-300). The EIS results remain stable over 32 days as shown in Fig. 11b with no observed signs of electrode degradation. Based on previous literature, the resulting electrode-electrolyte impedance of our Pt microelectrode is low enough to capture the electrophysiology of neurons with a signal attenuation of less than 25% [76, 77].

B. *Chip Packaging for On-CMOS Cell Culturing*

After completion of the CMOS post-processing and surface compatibility verification, the chip is wire-bonded to an FR-4 PCB board as the daughterboard. The wire bonds and chip pads are then encapsulated using medical epoxy to mechanically secure the wire bonds to the chip and PCB pads while isolating them from the culture medium, preventing undesired chemical reactions. For cell culturing, we attach a 35 mm diameter borosilicate culture dish via PDMS over the chip. To further improve biocompatibility and protection, a final layer of PDMS is coated over the region between the chip and the dish edge. Hence, with our in-house CMOS post-processing and packaging processes, the CMOS multi-modal cellular interface array achieves excellent biocompatibility that supports stable long-term on-chip cell culture and cellular measurements. The die microphotograph and the packaged daughterboard with only the active array region exposed are shown in Fig. 10.

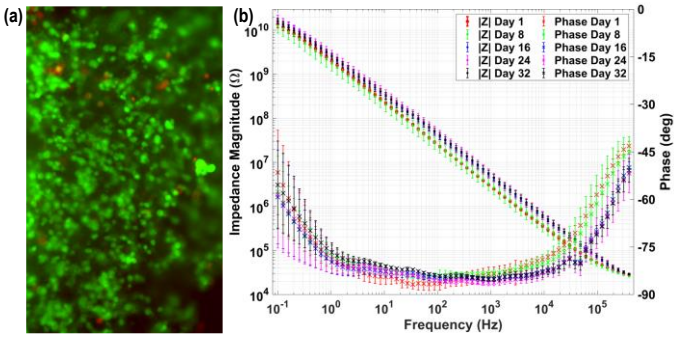

Fig. 11. Long-term biocompatibility and chemical stability of post-processed pixel array. (a) Live/dead analysis of on-chip cultured hydrogel encapsulating SNaPs over a month. Green indicated viable cells while red labels dead cells. (b) Long-term EIS measurements of on-chip 8.84 μm × 11 μm Pt electrode.

C. *Measurement Setup for Biological Experimentation*

During testing, the daughter PCB board containing the completely packed CMOS cellular interfacing array is linked to a PCB motherboard, which supplies the supply voltages and other reference voltages essential for the CMOS chip's operation. A custom-made LabVIEW interface programs the National Instruments (PXI-6541) 50 MHz waveform generator/analyzer which delivers the control signal to the on-chip SPI to control the chip's processes and obtains the digital output data. The arbitrary waveform generator (Keysight 81160A) provides the clock signal and ZS modality's Z-CLK.

For the biological measurements, we fabricate hydrogels encapsulating human stem cell-derived neurogenin 2-accelerated progenitor cells (SNaPs) and attach them over the CMOS cellular interface array. The cells are differentiated for 4 weeks to build the *in vitro* on-chip brain model [78, 79]. The procedures for inducing SNaPs and printing mini-brains were previously reported [79, 80]. In short, the SNaPs (1×107 cells mL^{-1}) were mixed with GelMA/HAMA (2.5%/1.5%) and 1-mM/10-mM Ru/SPS as the bioink to bioprint the brain mimicking hydrogel constructs (cubes of $4 \times 4 \times 2$ mm^3). The printed construct is transferred to the active sensing area of the CMOS cellular interfacing array for long-term culturing. The bioprinted SNaPs are cultured on the cellular interfacing array for over 4 weeks with the maintenance medium [79] changed every day. The multidimensional physiological responses are recorded by our CMOS cellular interfacing array after 4 weeks with and without BCS actuation from our platform.

For digital pathology studies, pathogen infection experiments are conducted using COVID-19 pseudo particles transfecting the SNaPs in the mini-brains where massive electrophysiological data are recorded and digitized for future diagnosis and analysis. Moreover, a differentiated C2C12 mouse skeletal myoblast (CRL-1772, ATCC) monolayer is cultured over the active sensing area of the CMOS cellular interface array. The monolayer is sustained for 7 days in Dulbecco's modified Eagle medium (DMEM, ThermoFisher) supplemented with 10 v/v% fetal bovine serum (FBS, Gibco, USA) and 1 v/v% antibiotic-antimycotic (Gibco) for adherence analyses and to verify the culture biocompatibility of the CMOS cellular interfacing array.

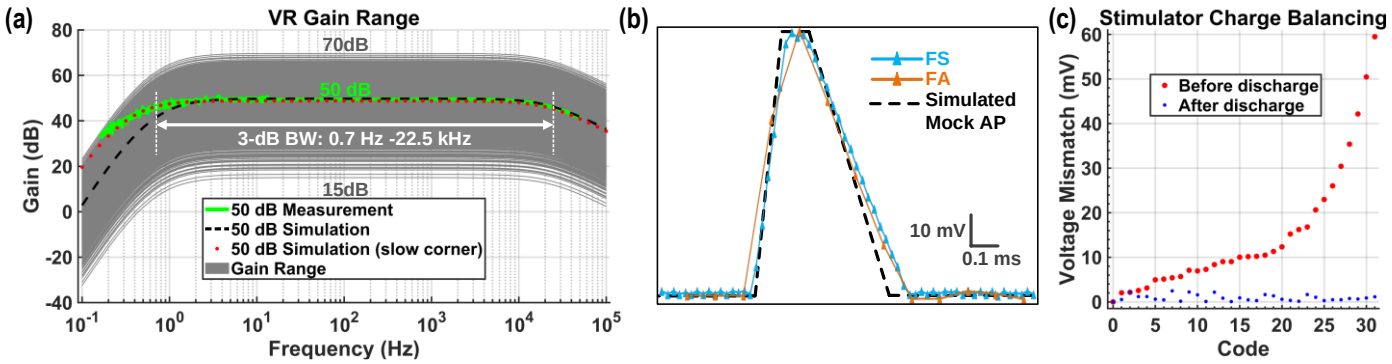

Fig. 12. (a) VR gain range with measured gain overlapping simulated gain for nominal (black dash) and slower (red dot) devices at 50 dB gain settings. (b) FS and FA recording of a mock AP produced by a waveform generator. (c) Voltage mismatch before and after charge balancing during BCS.

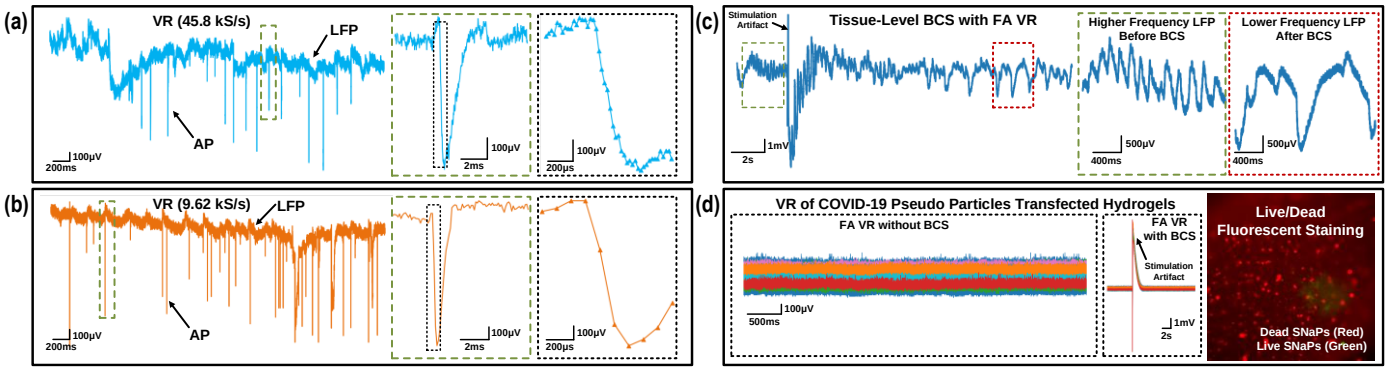

Fig. 13. Programmable sampling rates utilized by (a) FS and (b) FA VR modality showing more information on the sharp changes in electrophysiology during an action potential from hydrogel encapsulating SNaPs. (c) Tissue-level BCS during FA VR of SNaPs. (d) Overlapped FA VR from multiple parallel pixels with and without tissue-level BCS of SNaPs transfected with COVID-19 pseudo particles showing inhibited potentials with live/dead analysis.

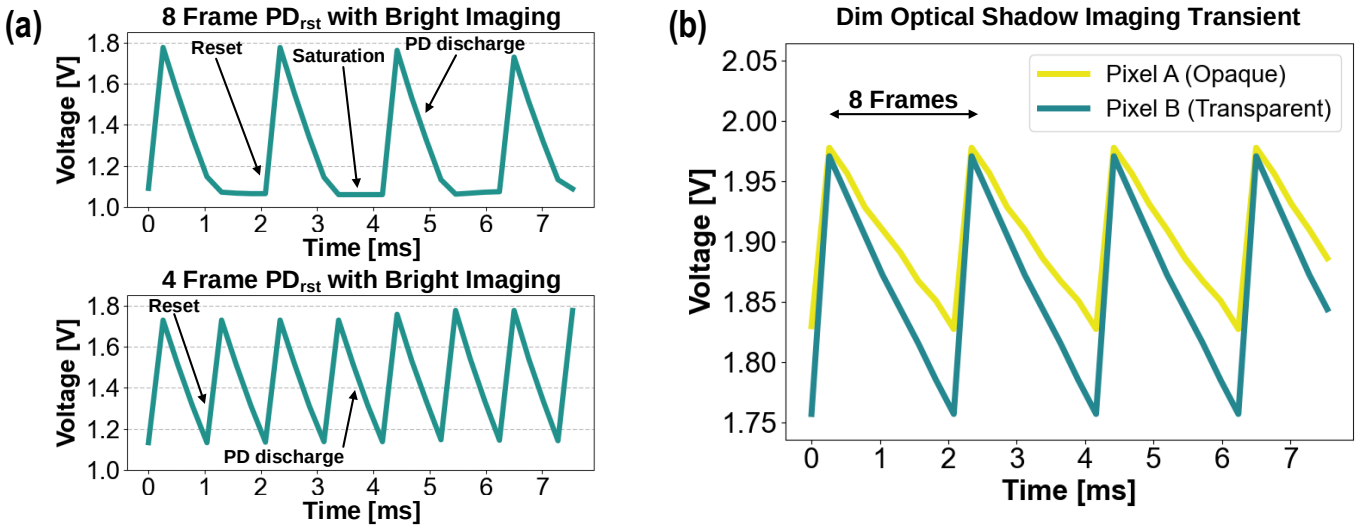

Fig. 14. (a) Comparison of PD voltage transient operating under dim (top) and bright (bottom) OD when exposed to stereo microscope LED at the brightest setting. (b) Comparison of PD voltage transient during dim OD between pixels overshadowed and not covered by C2C12 cells.

IV. Electrical And Biological Measurements

To demonstrate the multi-modal/-functional cellular sensing/actuating array, we have performed extensive electrical, cell-based assays, and organ-on-chip measurements. To characterize the VR modality, the voltage gain is simulated to show the gain ranges from 15 dB to 70 dB and a dynamic signal analyzer (Keysight 35670A) measures the gain setting at 50 dB, an appropriate gain for neuron LFP and APs, which is compared to the simulated value as illustrated in Fig. 12a. The discrepancy in the roll-off around the high-pass corner for the measured 50 dB gain setting compared to the typical 50 dB simulated gain can be attributed to process variation with slower devices which can increase the resistance of the pseudo-resistors, lowering the cut-off frequency. Additionally, the VR modality set at 15 dB gain can faithfully capture a mock intracellular AP constructed by Keysight 81160A which is fed into a test pixel as depicted in Fig. 12b. The measured charge balancing of the stimulator is shown in Fig. 12c, where the switch S_{dis} uses the voltage $VBias_{stim}$ to discharge residual

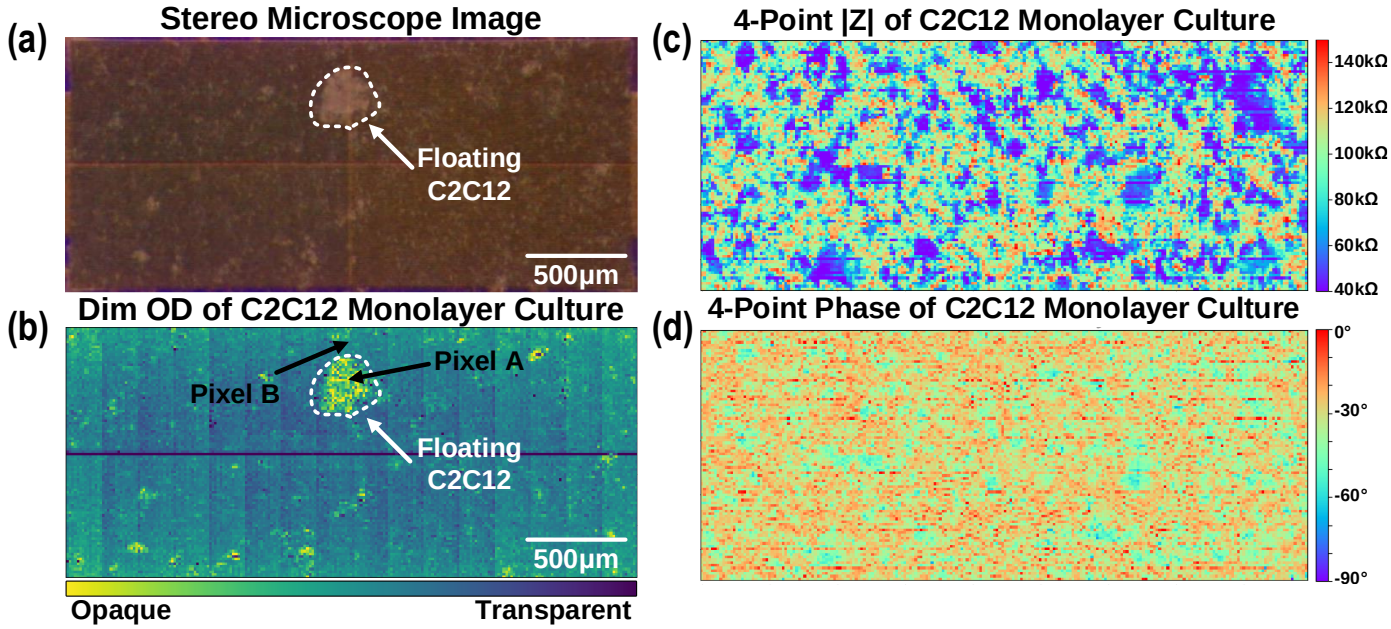

Fig. 15. Biological demonstration using C2C12 monolayer culture. (a) Stereo microscope image over sensing area. (b) Dim OD imaging. (c) 4-point impedance magnitude mapping. (c) 4-point impedance phase mapping.

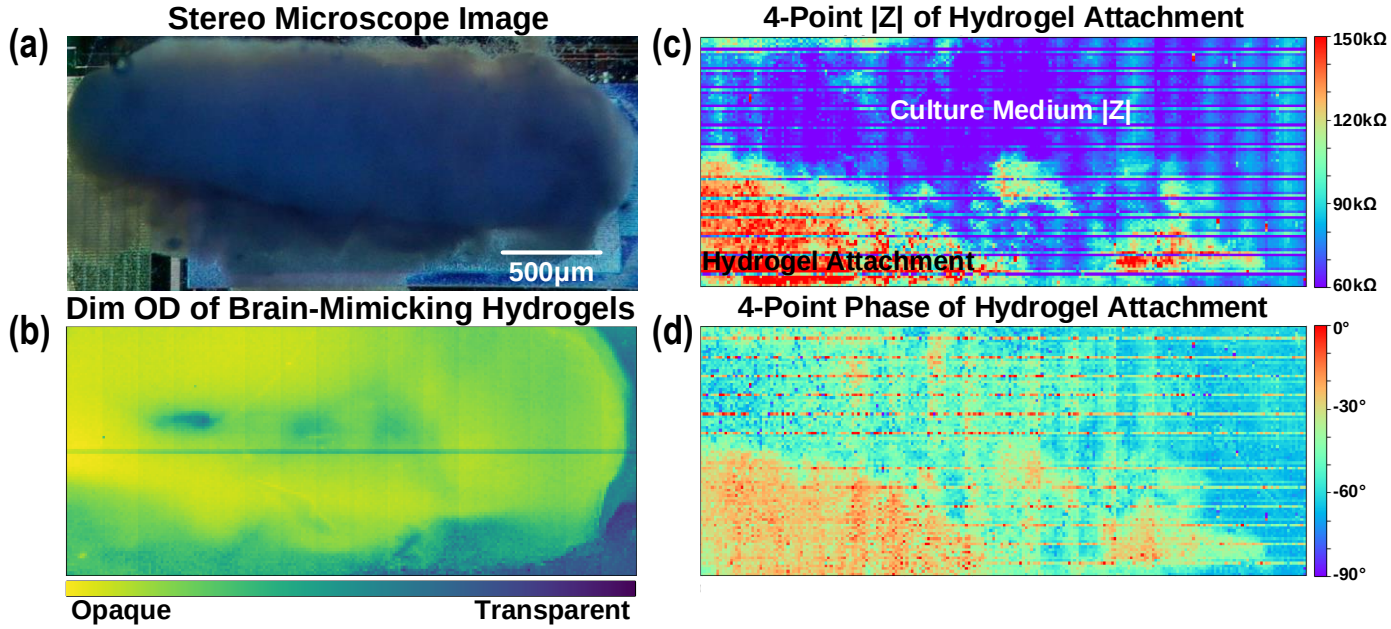

Fig. 16. Biological demonstration using brain mimicking hydrogel encapsulating SNaPs. (a) Stereo microscope image over sensing area. (b) Dim OD imaging. (c) 4-point impedance mapping for the amplitude of the cellular impedance. (c) 4-point impedance mapping for the phase of the cellular impedance.

charge on the electrodes after BCS from the slightly unbalanced anodic and cathodic currents. The average voltage mismatch after applying a charge-balancing discharge pulse across all stimulator codes was shown to be less than 1 mV. We have measured the APs and LFPs from the brain-mimicking hydrogels using both FA (9.62 kHz sampling) and FS (45.8 kHz sampling) VR at 54.3dB gain shown in Fig. 13a,b, demonstrating that the FS mode captures the sharp spikes of extracellular LFPs and APs more precisely. To demonstrate the simultaneous BCS and VR modalities, tissue-level BCS with 340uA with an anodic current, delay, and cathodic current, each for 200µs is applied during FA VR in which frequency alterations in LFPs are observed after excitation as shown in Fig. 13c. The current amplitude of 340 µA was chosen here for tissue-level stimulation to ensure that the sample will be excited as the 98 pixels within a pixel bank will share the output current for ideally 3.47 µA per channel. However, due to the nature of culturing, the sample cannot evenly adhere across the array, therefore the resulting current delivered to the sample will be lower than expected. With a higher current, the chances of exciting the cells within the hydrogel are maximized. We have also transfected the brain-mimicking hydrogel with COVID-19 pseudo particles and evaluated the potential response after 48 hours, where we find that neurons' APs/LFPs are diminished as

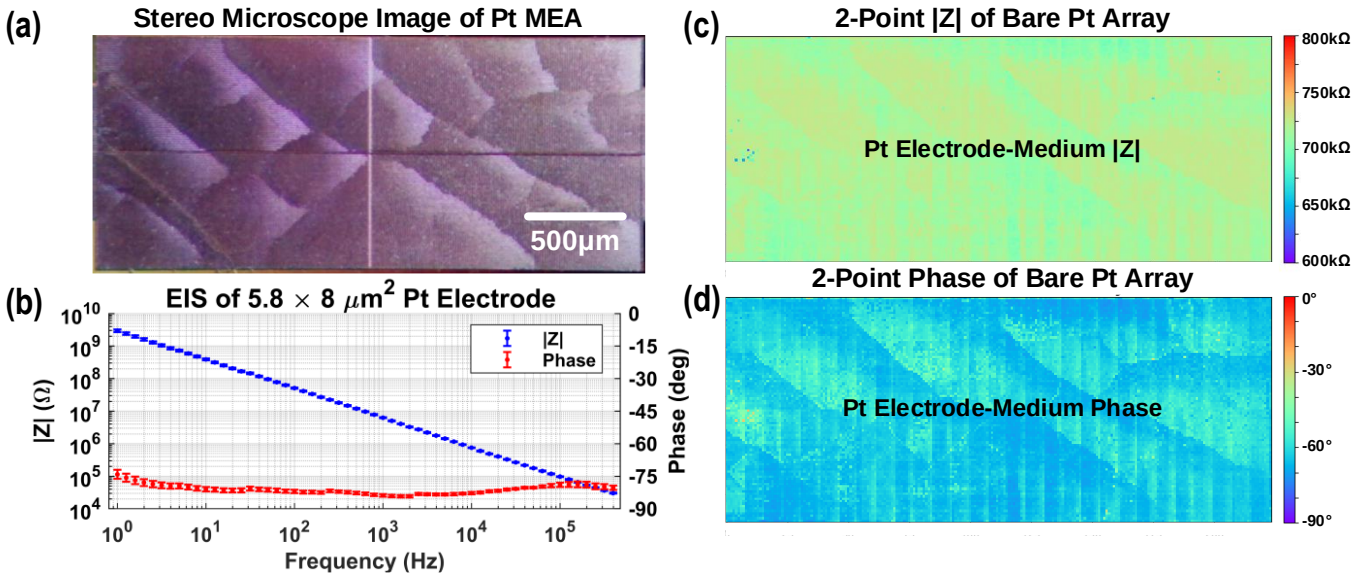

Fig. 17. (a) Stereo microscope image over sensing area EBPVD Pt MEA. (b) EIS measurement of on-chip electrode. (c) 2-point impedance magnitude mapping (d) 2-point impedance phase mapping.

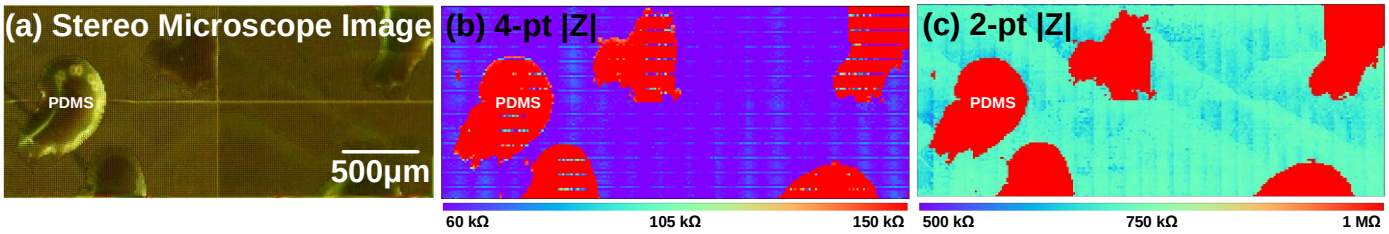

Fig. 18. Demonstration of ZS using cured PDMS droplets. (a) Stereo microscope image over sensing area. (b) 4-point impedance magnitude mapping. (c) 2-point impedance magnitude mapping.

indicated in Fig. 13d. Furthermore, we have performed VR while stimulating the COVID-19 infected samples with tissue-level BCS and observed the same suppressed potentials which are supported by live/dead fluorescent staining (Fig. 13d), revealing that most of the SNaPs have perished.

To characterize the photodiode responses during OD modality under 4-frame (bright) and 8-frame (dim) settings, the chip is subjected to a microscope LED (Leica EZ4) using the brightest setting. A comparison of 4-/8-frame PD_{rst} is presented in Fig. 14, demonstrating the steep transient voltage slope response of the PD for both bright/dim functionalities followed by saturation of the PD employing the 8-frame PD_{rst} due to the bright lighting. For biological verification, chips culturing the differentiated C2C12 mouse myoblast monolayer in Fig. 15 and brain-mimicking hydrogels in Fig. 16 are subjected to the microscope LED (Leica EZ4) using the dimmest setting. Utilizing the dim OD, the resulting optical shadowing images of both the hydrogel and C2C12 monolayer closely correspond with the stereomicroscope images as illustrated in Fig. 15 and Fig. 16, revealing sample transparency, morphology, and location. Fig. 14b shows the differences in transient voltage slopes between a pixel overshadowed and not covered by the C2C12 culture. Particularly for the hydrogel sample, the more transparent areas are especially highlighted by the OD which is not easily distinguished utilizing a stereomicroscope.

To visualize the ZS modality, impedance magnitude and phase mappings at 25 kHz are constructed from the 21,952 pixels. The 2-point ZS is validated using a special test chip in a culture medium without any biological samples. Here, the specific CMOS chip consists of smaller electrodes (5.8 µm × 8 µm) with Pt deposited via EBPVD. The smaller electrodes in this test chip can be attributed to the directional deposition nature of EBPVD whereas sputtering results in conformal coating. EVPVD, thus, will be unable to coat the undercut of the bilayer photolithography. As described earlier, EBPVD consists of high temperatures which will result in processing nonuniformities on-chip. We deliberately use EBPVD here to induce deposition inconsistencies which can be optically observed in Fig. 17a, causing slight fluctuations in impedance. The resulting pixel array will have slight surface variation which is highlighted in 2-point ZS in Fig. 17c,d. When utilizing 2-point ZS with an excitation signal of 25 kHz, the resulting magnitude and phase mappings well resemble the stereomicroscope image and closely match the two electrode-medium interfacial impedance in series at 25 kHz (~700 kΩ). Afterward, to further assess the ZS validity, we place a few drops of PDMS on the test chip to mimic as high impedance cellular clusters as shown in Fig. 18. Both the resulting 2-point and 4-point mappings accurately capture the high-impedance zones, as the mappings closely match the stereomicroscope image. As expected, the 4-point impedance mapping eliminates the C_{dl} and R_C, leaving behind $2R_S$ (~65 kΩ). For biological experimentation, brain-mimicking hydrogels in Fig. 16 and C2C12 mouse myoblast sample in Fig. 15 are 4-point ZS mapped to clearly show the sample adhesion. Impedance imaging is required because it can sometimes be challenging to monitor cells growing in a monolayer across a dense pixel array using standard optical imaging. The combination of OD and ZS

TABLE 1
COMPARISON TABLE OF STATE-OF-THE-ART CMOS BIOSENSORS

Reference	This Work	[14]	[15]	[42]	[43]	[51]	[54]	[81]	[82]	[83]
Modalities	Voltage Recording, Optical Detection, Impedance Sensing, Biphasic Current Stimulation	VR, OD, ZS, I-Stim,	VR, I-/V-Stim	VR, I-/V-Stim	VR, ZS, I-/V-Stim	VR, I-Stim, OD, ZS	VR, ZS	VR, ZS, I-/V-Stim	VR, ZS, I-Stim	VR, V-Stim
Reconfigurable VR Scan Rate	Yes	No	No	Yes	No	No	No	No	No	No
Dim/Bright OD	Yes	No	No	No	No	No	No	No	No	No
2-/4-pt Impedance Sensing	Yes	Yes	No	No	No	No	No	No	No	No
Single-Cell/Tissue-Level Stimulation	Yes	No	Yes	No	No	No	No	No	No	No
VR Sampling Rate (kHz)	9.62 (Full Array) 45.8 (Fast Scan)	3.84	9.4	11.6 (Full Array) 24.4 (Switch Matrix)	20	15	20	10	10	14
VR Gain (dB)	15 – 70	33.3 – 52.5	29.5 – 48.7	38.9 – 76.4	6 – 69.5	52.3	58.54	-	40 – 62	54 – 73
Maximum Concurrent Stimulation Pixels	1568	64	4096	8	64	4	-	16	-	-
Number of Concurrent Recording Channels	1568 VR (Full Array) 304 VR (Fast Scan) 1568 OD 16 ZS	1568 VR 1568 OD 16 ZS	4096	19584 (Full Array) 246 (Switch Matrix)	1024	4	2048 VR 32 ZS	64 VR + ZS	16 VR 48 ZS	128
Total Number of Pixels	21952	21952	4096	19584	16384	1024	59760	64	-	-
Pixel Pitch (µm)	13	16	20	18	15	58	13.5	140**	-	-
Electrode Density (# pixels/mm^2)*	5893 (Full Array) 1142 (Fast Scan)	3811	1538	3050 (Full Array) 38 (Limited Pixels)	4444	299	5489	38**	-	-
Active Area (mm^2)	2.91 × 1.28	3.6 × 1.6	1.27 × 1.27	3.5 × 1.8	16 × (0.48 × 0.48)	1.85 × 1.85	4.5 × 2.4	1.3 × 1.3**	-	-
Electrode Material	Ti/Pt	Ti/Au	Al/Ti/Pt/PtB	Al/TiW/Pt/PtB	Al/Ti/TiN	Al/Zn/Ni/Au	Al/TiW/Pt/PtB	Au	External Electrodes	External Electrodes
Assay Type	SNaPs†, C2C12‡	Cardiomyocytes, Fibroblast	Neurons, Cardiomyocytes	Primary Neurons, Hippocampal Slices, Cardiomyocytes	Cardiomyocytes	Rat Cardiomyocytes	Cardiac, Brain Slices	Rat Peripheral Nerves	Rat Spinal Cord	Neurons
Input-referred Noise for VR (μV_{rms})	10.5 (1 – 300 Hz) 4.35 (300 – 3.3k Hz)	10.3 (1 – 400 Hz) 3.65 (401 – 2.3k Hz)	23 (1 – 4.7k Hz) 5.6 (300 – 10k Hz)	3.0 (Switch Matrix) (300 – 5k Hz) 10.4 (Full Array) (300 – 5k Hz)	12 (0.5 – 10k Hz) 7.5 (300 – 10k Hz)	11.7 (1 – 300 Hz) 7.08 (300 – 6k Hz)	3.6 (1 – 300 Hz) 2.4 (300 – 10k Hz)	24.76 (1 – 10k Hz)	7.68 (5 – 10k Hz)	6.08 (10 – 5k Hz)
ADC Resolution (ENOB)	9.15	9.15	External ADC	8.4	8.16	External ADC	N/A	8	8.5	6.2
Power (mW)	1400 (VR) 168 (OD) 182 (Z)	690 (VR) 90 (OD) 60 (Z)	1250	125	95	N/A	86	0.81	18	2.4 (VR) 7 (V-Stim)
Tech. (nm)	130	130	180	180	130	130	180	130	180	350

* Electrode Density = (Total Number of Pixels)/(Active Area)
** Estimated
† SNaPs: human stem cell-derived neurogenin 2-accelerated progenitor cells, which were differentiated for 4 weeks
‡ C2C12: mouse skeletal myoblast differentiated into muscle cells

can distinguish between attached and floating cells in near-transparent cell monolayers, allowing the multi-modal cellular interfacing array to be employed in a variety of cell cultures. With all four dual functional modalities, the multi-modality array effectively displays cell-based assessments with an excellent resolution with rapid scan rates.

V. CONCLUSION

In summary, we present a multimodal and multifunctional CMOS cellular interfacing array with high-density pixels with single-cell resolution in a tissue-level FOV and adjustable sampling rate to achieve both high throughput and sensitivity for comprehensive cellular characterization in digital physiology and pathology applications. Our CMOS cellular interfacing array contains up to 1,568 parallel readout channels over 21,952 individually addressable pixels with a 13 µm center-to-center pitch, the smallest reported multimodal sensing pixel containing a PD. Each modality is reconfigurable to perform different functions e.g. FA/FS VR, dim/bright OD, 2-/4-point ZS mapping, and single-cell/tissue-level BCS as well as achieving an extraordinarily high VR sampling speed (45.8 kHz/pixel). Having all these different multi-functional modalities integrated on a single chip allows for greater flexibility in serving a wide range of applications with varying needs. We have devised and optimized a high-yield post-CMOS processing procedure to fabricate an extremely biocompatible and stable electrode array on-chip while minimizing the electrode-electrolyte interfacial impedance to support long-term biological measurements. Our electrical tests and biological measurements utilizing on-chip cultured brain modeling hydrogels encapsulating SNaPs and C2C12 mouse skeletal myoblast monolayers successfully demonstrate the different multifunctional modalities of our platform. Table 1 compares our platform with the various state-of-the-art CMOS cellular assays along with multi-channel recording systems that do not employ a switching matrix [81-83]. Our CMOS cellular interface array boasts a reconfigurable scan rate versus FOV of

up to an extremely fast 45.8 kS/s, unprecedently high-density, and area-efficient multifunctional multimodal pixel array with 5893 pixels/mm^2, where our platform can readily extract different cellular physiological features with sharp features for long periods for holistic cellular and tissue characterizations, paving a paradigm shift in the disciplines of digital physiology and pathology.

ACKNOWLEDGMENTS

The authors thank the members of the Georgia Tech Electronics and MicroSystem (GEMS) Lab and ETH Zurich's Integrated Devices, Electronics, And Systems (IDEAS) Group for their helpful discussions. We also thank Globalfoundries for MPW chip fabrications. A.W. is grateful for the financial support of this research through the National Defense Science and Engineering Graduate Fellowship sponsored by the Department of Defense (F-7863984656).

REFERENCES

[1] L. Pantanowitz, "Digital images and the future of digital pathology," (in eng), *J Pathol Inform*, vol. 1, Aug 10 2010.

[2] S. Al-Janabi *et al.*, "Digital pathology: current status and future perspectives," *Histopathology*, vol. 61, no. 1, pp. 1-9, 2012.

[3] J. Griffin and D. Treanor, "Digital pathology in clinical use: where are we now and what is holding us back?," *Histopathology*, vol. 70, no. 1, pp. 134-145, 2017.

[4] H. Wallace and R. Angus, "Supplemental Learning in Respiratory Physiology for Healthcare Professionals Towards Successful Treatment of COVID-19," (in English), *Frontiers in Physiology*, Perspective vol. 12, no. 518, 2021-April-20 2021.

[5] A. Cimadamore *et al.*, "Digital pathology and COVID-19 and future crises: pathologists can safely diagnose cases from home using a consumer monitor and a mini PC," (in eng), *J Clin Pathol*, vol. 73, no. 11, pp. 695-696, Nov 2020.

[6] M. G. Hanna *et al.*, "Validation of a digital pathology system including remote review during the COVID-19 pandemic," *Modern Pathology*, vol. 33, no. 11, pp. 2115-2127, 2020/11/01 2020.

[7] S. Taheri-Araghi *et al.*, "Single-Cell Physiology," (in eng), *Annu Rev Biophys*, vol. 44, pp. 123-42, 2015.

[8] J. Park *et al.*, "11.7 A multimodality CMOS sensor array for cell-based assay and drug screening," in *2015 IEEE International Solid-State Circuits Conference - (ISSCC) Digest of Technical Papers*, 2015, pp. 1-3.

[9] T. Chi *et al.*, "A Multi-Modality CMOS Sensor Array for Cell-Based Assay and Drug Screening," *IEEE Transactions on Biomedical Circuits and Systems*, vol. 9, no. 6, pp. 801-814, 2015.

[10] N. Li *et al.*, "High throughput slanted scanning whole slide imaging system for digital pathology," *Journal of Biophotonics*, vol. 14, no. 6, p. e202000499, 2021.

[11] J. M. Rothberg *et al.*, "An integrated semiconductor device enabling non-optical genome sequencing," *Nature*, vol. 475, no. 7356, pp. 348-352, 2011/07/01 2011.

[12] X. Huang *et al.*, "A Dual-Mode Large-Arrayed CMOS ISFET Sensor for Accurate and High-Throughput pH Sensing in Biomedical Diagnosis," *IEEE Transactions on Biomedical Engineering*, vol. 62, no. 9, pp. 2224-2233, 2015.

[13] H. Wang *et al.*, "Cell culture and cell based sensor on CMOS," in *2014 IEEE Biomedical Circuits and Systems Conference (BioCAS) Proceedings*, 2014, pp. 468-471.

[14] D. Jung *et al.*, "A CMOS 21 952-Pixel Multi-Modal Cell-Based Biosensor With Four-Point Impedance Sensing for Holistic Cellular Characterization," *IEEE Journal of Solid-State Circuits*, vol. 56, no. 8, pp. 2438-2451, 2021.

[15] J. Abbott *et al.*, "The Design of a CMOS Nanoelectrode Array With 4096 Current-Clamp/Voltage-Clamp Amplifiers for Intracellular Recording/Stimulation of Mammalian Neurons," *IEEE Journal of Solid-State Circuits*, vol. 55, no. 9, pp. 2567-2582, 2020.

[16] S. R. Kumashi *et al.*, "A CMOS Multi-Modal Electrochemical and Impedance Cellular Sensing Array for Massively Paralleled Exoelectrogen Screening," *IEEE Transactions on Biomedical Circuits and Systems*, pp. 1-1, 2021.

[17] J. S. Park *et al.*, "Intracellular cardiomyocytes potential recording by planar electrode array and fibroblasts co-culturing on multi-modal CMOS chip," *Biosensors and Bioelectronics*, vol. 144, p. 111626, 2019/11/01/ 2019.

[18] R. R. Harrison and C. Charles, "A low-power low-noise CMOS amplifier for neural recording applications," *IEEE Journal of Solid-State Circuits*, vol. 38, no. 6, pp. 958-965, 2003.

[19] A. Caboni *et al.*, "Integration of a microfluidic flow cell on a CMOS biosensor for DNA detection," in *2008 Ph.D. Research in Microelectronics and Electronics*, 2008, pp. 121-124.

[20] Y.-Z. Juang *et al.*, "CMOS Biomedical Sensor with In Situ Gold Reference Electrode for Urine Detection Application," *Procedia Engineering*, vol. 47, pp. 1005-1008, 2012/01/01/ 2012.

[21] V. D. Nguyen *et al.*, "A handheld-type total integrated capillary electrophoresis system for SARS-CoV-2 diagnostics: Power, fluorescence detection, and data analysis by smartphone," *Biosensors and Bioelectronics*, vol. 195, p. 113632, 2022/01/01/ 2022.

[22] T. Shaffaf *et al.*, "Towards Fully Integrated Portable Sensing Devices for COVID-19 and Future Global Hazards: Recent Advances, Challenges, and Prospects," *Micromachines*, vol. 12, no. 8, 2021.

[23] S. Forouhi and E. Ghafar-Zadeh, "Applications of CMOS Devices for the Diagnosis and Control of Infectious Diseases," *Micromachines*, vol. 11, no. 11, 2020.

[24] H. Wang *et al.*, "A frequency-shift CMOS magnetic biosensor array with single-bead sensitivity and no external magnet," in *2009 IEEE International Solid-State Circuits Conference - Digest of Technical Papers*, 2009, pp. 438-439,439a.

[25] A. M. Ghaemmaghami *et al.*, "Biomimetic tissues on a chip for drug discovery," *Drug Discovery Today*, vol. 17, no. 3, pp. 173-181, 2012/02/01/ 2012.

[26] Y. S. Zhang *et al.*, "Google Glass-Directed Monitoring and Control of Microfluidic Biosensors and Actuators," *Scientific Reports*, vol. 6, no. 1, p. 22237, 2016/03/01 2016.

[27] S. B. Kim *et al.*, "A cell-based biosensor for real-time detection of cardiotoxicity using lensfree imaging," 10.1039/C1LC20098D vol. 11, no. 10, pp. 1801-1807, 2011.

[28] U. Shin *et al.*, "A 256-Channel 0.227µJ/class Versatile Brain Activity Classification and Closed-Loop Neuromodulation SoC with 0.004mm^2-1.51 µW/channel Fast-Settling Highly Multiplexed Mixed-Signal Front-End," in *2022 IEEE International Solid- State Circuits Conference (ISSCC)*, 2022, vol. 65, pp. 338-340.

[29] U. Shin *et al.*, "A 16-Channel 60µW Neural Synchrony Processor for Multi-Mode Phase-Locked Neurostimulation," in *2022 IEEE Custom Integrated Circuits Conference (CICC)*, 2022, pp. 01-02.

[30] M. Shoaran *et al.*, "A 16-channel 1.1mm2 implantable seizure control SoC with sub- µ W/channel consumption and closed-loop stimulation in 0.18µm CMOS," in *2016 IEEE Symposium on VLSI Circuits (VLSI-Circuits)*, 2016, pp. 1-2.

[31] M. Shoaran *et al.*, "Compact Low-Power Cortical Recording Architecture for Compressive Multichannel Data Acquisition," *IEEE Transactions on Biomedical Circuits and Systems*, vol. 8, no. 6, pp. 857-870, 2014.

[32] M. Schienle *et al.*, "A fully electronic DNA sensor with 128 positions and in-pixel A/D conversion," *IEEE Journal of Solid-State Circuits*, vol. 39, no. 12, pp. 2438-2445, 2004.

[33] A. Manickam *et al.*, "A CMOS Electrochemical Impedance Spectroscopy (EIS) Biosensor Array," *IEEE Transactions on Biomedical Circuits and Systems*, vol. 4, no. 6, pp. 379-390, 2010.

[34] G. Medoro *et al.*, "A lab-on-a-chip for cell detection and manipulation," *IEEE Sensors Journal*, vol. 3, no. 3, pp. 317-325, 2003.

[35] B. Jang *et al.*, "A CMOS fluorescent-based biosensor microarray," in *2009 IEEE International Solid-State Circuits Conference - Digest of Technical Papers*, 2009, pp. 436-437,437a.

[36] G. Patounakis *et al.*, "Active CMOS Array Sensor for Time-Resolved Fluorescence Detection," *IEEE Journal of Solid-State Circuits*, vol. 41, no. 11, pp. 2521-2530, 2006.

[37] H. Wang, "Magnetic Sensors for Diagnostic Medicine: CMOS-Based Magnetic Particle Detectors for Medical Diagnosis Applications," *IEEE Microwave Magazine*, vol. 14, no. 5, pp. 110-130, 2013.

[38] H. Wang *et al.*, "A magnetic cell-based sensor," *Lab on a Chip*, vol. 12, no. 21, pp. 4465-4471, 2012.

[39] B. Alberts *et al.*, *Molecular biology of the cell*, 4th ed. ed. New York: Garland Science (in English), 2002.

[40] D. J. Randall *et al.*, *Eckert animal physiology : mechanisms and adaptations*, Ed. 5. ed. New York: W.H. Freeman and Co. (in English), 2002.
[41] M. Ballini *et al.*, "A 1024-Channel CMOS Microelectrode Array With 26,400 Electrodes for Recording and Stimulation of Electrogenic Cells In Vitro," *IEEE Journal of Solid-State Circuits*, vol. 49, no. 11, pp. 2705-2719, 2014.
[42] X. Yuan *et al.*, "Extracellular Recording of Entire Neural Networks Using a Dual-Mode Microelectrode Array With 19 584 Electrodes and High SNR," *IEEE Journal of Solid-State Circuits*, vol. 56, no. 8, pp. 2466-2475, 2021.
[43] C. M. Lopez *et al.*, "A Multimodal CMOS MEA for High-Throughput Intracellular Action Potential Measurements and Impedance Spectroscopy in Drug-Screening Applications," *IEEE Journal of Solid-State Circuits*, vol. 53, no. 11, pp. 3076-3086, 2018.
[44] C. M. Lopez *et al.*, "A 16384-electrode 1024-channel multimodal CMOS MEA for high-throughput intracellular action potential measurements and impedance spectroscopy in drug-screening applications," in *2018 IEEE International Solid - State Circuits Conference - (ISSCC)*, 2018, pp. 464-466.
[45] A. Wang *et al.*, "A CMOS Cellular Interface Array for Digital Physiology Featuring High-Density Multi-Modal Pixels and Reconfigurable Sampling Rate," in *International Solid-State Circuits Conference, under review*, 2022.
[46] J. Park *et al.*, "A CMOS 22k-pixel single-cell resolution multi-modality real-time cellular sensing array," in *2017 IEEE Custom Integrated Circuits Conference (CICC)*, 2017, pp. 1-4.
[47] D. Jung *et al.*, "A 21952-Pixel Multi-Modal CMOS Cellular Sensor Array with 1568-Pixel Parallel Recording and 4-Point Impedance Sensing," in *2019 Symposium on VLSI Circuits*, 2019, pp. C62-C63.
[48] J. Park *et al.*, "A high-density CMOS multi-modality joint sensor/stimulator array with 1024 pixels for holistic real-time cellular characterization," in *2016 IEEE Symposium on VLSI Circuits (VLSI-Circuits)*, 2016, pp. 1-2.
[49] W. P. Chan *et al.*, "A pressure/oxygen/temperature sensing SoC for multimodality intracranial neuromonitoring," in *2013 IEEE Asian Solid-State Circuits Conference (A-SSCC)*, 2013, pp. 89-92.
[50] C. Li *et al.*, "A novel lab-on-a-tube for multimodality neuromonitoring of patients with traumatic brain injury (TBI)," *Lab on a Chip*, vol. 9, no. 14, pp. 1988-1990, 2009.
[51] J. Park *et al.*, "1024-Pixel CMOS Multimodality Joint Cellular Sensor/Stimulator Array for Real-Time Holistic Cellular Characterization and Cell-Based Drug Screening," *IEEE Transactions on Biomedical Circuits and Systems*, vol. 12, no. 1, pp. 80-94, 2018.
[52] J. S. Park *et al.*, "Multi-parametric cell profiling with a CMOS quad-modality cellular interfacing array for label-free fully automated drug screening," *Lab on a Chip*, vol. 18, no. 19, pp. 3037-3050, 2018.
[53] Y.-T. Chen *et al.*, "Review of Integrated Optical Biosensors for Point-of-Care Applications," *Biosensors*, vol. 10, no. 12, 2020.
[54] V. Viswam *et al.*, "Impedance Spectroscopy and Electrophysiological Imaging of Cells With a High-Density CMOS Microelectrode Array System," *IEEE Transactions on Biomedical Circuits and Systems*, vol. 12, no. 6, pp. 1356-1368, 2018.
[55] A. Mucha *et al.*, "Sensing cellular adhesion with a CMOS integrated impedance-to-frequency converter," in *2011 IEEE Sensors Applications Symposium*, 2011, pp. 12-17.
[56] T. Sun *et al.*, "On-chip electrical impedance tomography for imaging biological cells," *Biosensors and Bioelectronics*, vol. 25, no. 5, pp. 1109-1115, 2010/01/15/ 2010.
[57] M. Dipalo *et al.*, "Intracellular and Extracellular Recording of Spontaneous Action Potentials in Mammalian Neurons and Cardiac Cells with 3D Plasmonic Nanoelectrodes," *Nano Letters*, vol. 17, no. 6, pp. 3932-3939, 2017/06/14 2017.
[58] L. Berdondini *et al.*, "Active pixel sensor array for high spatio-temporal resolution electrophysiological recordings from single cell to large scale neuronal networks," *Lab on a Chip*, vol. 9, no. 18, pp. 2644-2651, 2009.
[59] B. Johnson *et al.*, "A 768-Channel CMOS Microelectrode Array With Angle Sensitive Pixels for Neuronal Recording," *IEEE Sensors Journal*, vol. 13, no. 9, pp. 3211-3218, 2013.
[60] B. Eversmann *et al.*, "A 128 × 128 CMOS biosensor array for extracellular recording of neural activity," *IEEE Journal of Solid-State Circuits*, vol. 38, no. 12, pp. 2306-2317, 2003.
[61] P. Ruther and O. Paul, "New approaches for CMOS-based devices for large-scale neural recording," *Current Opinion in Neurobiology*, vol. 32, pp. 31-37, 2015/06/01/ 2015.
[62] J. Navajas *et al.*, "Minimum requirements for accurate and efficient real-time on-chip spike sorting," (in eng), *J Neurosci Methods*, vol. 230, pp. 51-64, 2014.
[63] A. Marblestone* *et al.*, "Physical principles for scalable neural recording," (in English), *Frontiers in Computational Neuroscience*, Hypothesis and Theory vol. 7, 2013-October-21 2013.
[64] J. Icha *et al.*, "Phototoxicity in live fluorescence microscopy, and how to avoid it," (in eng), *Bioessays*, vol. 39, no. 8, Aug 2017.
[65] S. Senova *et al.*, "Experimental assessment of the safety and potential efficacy of high irradiance photostimulation of brain tissues," *Scientific Reports*, vol. 7, no. 1, p. 43997, 2017/03/09 2017.
[66] A. Wang *et al.*, "Electrode–Electrolyte Interface Impedance Characterization of Ultra-Miniaturized Microelectrode Arrays Over Materials and Geometries for Sub-Cellular and Cellular Sensing and Stimulation," *IEEE Transactions on NanoBioscience*, vol. 18, no. 2, pp. 248-252, 2019.
[67] A. Wang *et al.*, "Impedance Characterization and Modeling of Subcellular to Micro-sized Electrodes with Varying Materials and PEDOT:PSS Coating for Bioelectrical Interfaces," *ACS Applied Electronic Materials*, vol. 3, no. 12, pp. 5226-5239, 2021/12/28 2021.
[68] M. Ganji *et al.*, "Scaling Effects on the Electrochemical Performance of poly(3,4-ethylenedioxythiophene (PEDOT), Au, and Pt for Electrocorticography Recording," *Advanced Functional Materials*, vol. 27, no. 42, p. 1703018, 2017.
[69] C. C. Hsieh and M. D. Ker, "Monopolar Biphasic Stimulator With Discharge Function and Negative Level Shifter for Neuromodulation SoC Integration in Low-Voltage CMOS Process," *IEEE Transactions on Biomedical Circuits and Systems*, vol. 15, no. 3, pp. 568-579, 2021.
[70] L. Nguyen *et al.*, "Atomic-Scale Insights into the Oxidation of Aluminum," *ACS Applied Materials & Interfaces*, vol. 10, no. 3, pp. 2230-2235, 2018/01/24 2018.
[71] K. T. C. Chai *et al.*, "Modification of a CMOS microelectrode array for a bioimpedance imaging system," *Sensors and Actuators B: Chemical*, vol. 111-112, pp. 305-309, 2005/11/11/ 2005.
[72] S. Hwang *et al.*, "CMOS Microelectrode Array for Electrochemical Lab-on-a-Chip Applications," *IEEE Sensors Journal*, vol. 9, no. 6, pp. 609-615, 2009.
[73] A. Bonanno *et al.*, "A Multipurpose CMOS Platform for Nanosensing," (in eng), *Sensors (Basel)*, vol. 16, no. 12, Nov 30 2016.
[74] K. Niitsu *et al.*, "Development of Microelectrode Arrays Using Electroless Plating for CMOS-Based Direct Counting of Bacterial and HeLa Cells," *IEEE Transactions on Biomedical Circuits and Systems*, vol. 9, no. 5, pp. 607-619, 2015.
[75] V. Vijay *et al.*, "High-density CMOS microelectrode array system for impedance spectroscopy and imaging of biological cells," in *2016 IEEE SENSORS*, 2016, pp. 1-3.
[76] V. Viswam *et al.*, "Optimal Electrode Size for Multi-Scale Extracellular-Potential Recording From Neuronal Assemblies," (in English), *Frontiers in Neuroscience*, Original Research vol. 13, no. 385, 2019-April-26 2019.
[77] B. Miccoli *et al.*, "High-Density Electrical Recording and Impedance Imaging With a Multi-Modal CMOS Multi-Electrode Array Chip," (in English), *Frontiers in Neuroscience*, Original Research vol. 13, 2019-June-25 2019.
[78] C. Parra-Cantu *et al.*, "3D bioprinting of glioblastoma models," *Journal of 3D Printing in Medicine*, vol. 4, no. 2, pp. 113-125, 2020/06/01 2020.
[79] M. Wang *et al.*, "Molecularly cleavable bioinks facilitate high-performance digital light processing-based bioprinting of functional volumetric soft tissues," *Nature Communications*, vol. 13, no. 1, p. 3317, 2022/06/09 2022.
[80] M. F. Wells *et al.*, "Genome-wide screens in accelerated human stem cell-derived neural progenitor cells identify Zika virus host factors and drivers of proliferation," *bioRxiv*, p. 476440, 2018.
[81] M. ElAnsary *et al.*, "Bidirectional Peripheral Nerve Interface With 64 Second-Order Opamp-Less $\Delta\Sigma$ ADCs and Fully Integrated Wireless Power/Data Transmission," *IEEE Journal of Solid-State Circuits*, vol. 56, no. 11, pp. 3247-3262, 2021.
[82] Y. K. Lo *et al.*, "A Fully Integrated Wireless SoC for Motor Function Recovery After Spinal Cord Injury," *IEEE Transactions on Biomedical Circuits and Systems*, vol. 11, no. 3, pp. 497-509, 2017.
[83] F. Shahrokhi *et al.*, "The 128-Channel Fully Differential Digital Integrated Neural Recording and Stimulation Interface," *IEEE Transactions on Biomedical Circuits and Systems*, vol. 4, no. 3, pp. 149-161, 2010.

Adam Y. Wang (Student Member, IEEE) received the M.S. and Ph.D. degrees in electrical engineering from Georgia Institute of Technology, Atlanta, GA, USA in 2022 and the B.S. degree in electrical engineering and mathematics (Summa Cum Laude) from Vanderbilt University, Nashville, TN, USA in 2017. His research interests include bioelectronics, biomaterials, microfabrication, and integrated sensors for biomedical applications. Dr. Wang received the Analog Devices Outstanding Student Designer Award in 2020, National Defense Science and Engineering Graduate Fellowship in 2019, and the Presidential Fellowship from Georgia Institute of Technology in 2017.

Yuguo Sheng (Student Member, IEEE) received the B.S. degree in electrical engineering from the University of Michigan, Ann Arbor, USA, and the B.S. degree in electrical and computer engineering from Shanghai Jiao Tong University, Shanghai, China, both in 2020, and he received the M.S. degree in electrical and computer engineering from Georgia Institute of Technology, Atlanta, USA in 2021. He is currently working towards the Ph.D. degree in information technology and electrical engineering with the Swiss Federal Institute of Technology (ETH), Zürich, Switzerland. His research interests include bioelectronics, biomaterials, nanofabrication, molecular sensing, and integrated sensor systems.

Wanlu Li received her B.S. degree from Jilin University, China in 2015, and a Ph.D. in Biomedical Engineering at Shanghai Jiao Tong University, China. Dr. Li worked at Harvard Medical School as a visiting student and postdoctoral researcher (2018-2022). Since Aug 2022, she has been the tenure-track Assistant Professor at Biomedical Engineering School, Shanghai Jiao Tong University. Dr. Li's research is focused on innovating 3D bioprinting technologies to recreate functional tissues and their biomimetic models for applications in precision medicine. She has published over 30 papers in peer-reviewed journals, including Nature Communications, Advanced Materials, Aggregate, Advanced Healthcare Materials, and Biofabrication. Dr. Li received the Junior Investigator Award and Award for Scientific Excellence at the International Stroke Conference 2019 and International Society for Stem Cell Research (ISSCR) conference 2020.

Doohwan Jung (Member, IEEE) received the B.S. degree in electrical and electronic engineering from Yonsei University, Seoul, South Korea, in 2011, and the M.S. degree from the University of Michigan, Ann Arbor, MI, USA, in 2013, and the Ph.D. degree from the Georgia Institute of Technology, Atlanta, GA, USA, in 2020. From 2013 to 2015, he worked at Samsung Electronics, Seoul, where he designed PLL. His current research interests include novel RF, mm-wave integrated circuits, and sensors for biomedical applications. He received the Analog Devices Outstanding Student Designer Award, in 2018, and the CICC Best Student Paper Award, in 2019 (Second Place). His paper was selected for a Technical Tip Sheet at the 2019 VLSI Symposium.

Gregory V. Junek (Member, IEEE) received the B.S. degree in electrical engineering and computer science from the University of California at Berkeley, Berkeley, CA, USA, in 2018, and the M.S. degree in electrical and computer engineering from the Georgia Institute of Technology, Atlanta, GA, USA, in 2021. He is currently a member of the Georgia Tech Electronics and Micro-System (GEMS) Laboratory, Georgia Institute of Technology. His research takes place at the interface of biology, engineering, computer science, and physical sciences and addresses challenges in healthcare, precision medicine, and fundamental biological sciences. He is currently the Lead EE with OXOS Medical, Atlanta, where his team designs, develops, and manufactures cloud-connected medical imaging solutions, enabling medical professionals to determine radiographic diagnoses at the point of care.

Hangxing Liu (Student Member, IEEE) received the B.S. degree from Case Western Reserve University, Cleveland, OH, USA, in 2019, and the M.S. degree from the University of Pennsylvania, Philadelphia, PA, USA, in 2021. He is currently pursuing the Ph.D. degree with the Department of Information Technology and Electrical Engineering, ETH Zürich, Zürich, Switzerland. His current research interests include CMOS-based bioelectronics for cellular and molecular monitoring and implantable microsensors.

Jong-Seok Park (Member, IEEE) received the B.S. degree (Hons.) in electrical and electronic engineering from Yonsei University, Seoul, South Korea, in 2012, and the Ph.D. degree in electrical and computer engineering from the Georgia Institute of Technology, Atlanta, GA, USA, in 2017. He is currently with Intel Labs, Hillsboro, OR, USA. His current research interests include RF/millimeter-wave (mm-wave) integrated circuits and systems for wireless communications, integrated sensors/actuators for biomedical applications, and cryo-CMOS integrated systems for large-scale quantum qubit control. Dr. Park was a recipient of the Study-Abroad Scholarship from the Korea Foundation for Advanced Studies (KFAS) in 2012 and the Analog Device Inc. Outstanding Student Designer Award in 2014, the Catalyst Foundation, IBM, the Intel CICC Student Scholarship Award in 2015, and the CICC Best Student Paper Award in 2015. He was a co-recipient of the RFIC Best Student Paper Award (first place) in 2014.

Dongwon Lee (Student Member, IEEE) received the B.S. degree in electrical and electronic engineering from Yonsei University, Seoul, South Korea, in 2020, and the MS degree in electrical engineering from the Georgia Institute of Technology, Atlanta, GA, USA, in 2021. He is currently pursuing the Ph.D. degree in electrical engineering with ETH Zürich, Zürich, Switzerland. His current research interests include integrated biosensors and bioelectronics for cells and molecules, and RF/millimeter-wave (mm-wave) integrated circuits for communications.

Mian Wang received the B.S. degree in Biotechnology from Shandong University, China, in 2011, and M.S. degree in Mechanical engineering from George Washington University, Washington, D.C, USA, in 2013. He received the Ph.D. degree in Chemical Engineering from Northeastern University, Boston, MA, USA, in 2017, focusing on nanotechnology for tissue engineering and drug delivery. Before joining Tongji University, he worked as a postdoc at Harvard Medical School/Brigham and Women's Hospital, where he focused on innovating bioengineering approaches, including 3D bioprinting, organs-on-chips, and bioanalysis on recreating functional tissues/disease models, for applications in tissue regeneration and personalized medicine. He also serves as the associate editor of the International Journal of Nanomedicine (Dove Medical Press).

Sushila Maharjan received the M.S. degree in Chemistry from Tribhuvan University, Nepal, in 2003, and Ph.D. in Biochemistry from the Department of Life Science and Biochemical Engineering at Sun Moon University, Korea, in 2011. Her doctoral research focused on the genetic and metabolic engineering of biosynthetic pathways of antibiotics/anticancer drug production. She joined Seoul National University, Korea as a Postdoctoral Fellow in the Biomedical Polymers and Tissue Engineering laboratory where she was involved in the development and application of engineered biomaterials for targeted and controlled delivery of drugs and vaccines. She is currently a Postdoctoral Research Fellow at Brigham and Women's Hospital at Harvard Medical School. Her current interest is to study sex differences in diseases using organ-on-a-chip models.

Sagar R. Kumashi (Student Member, IEEE) received the B.Tech. and M.Tech. degrees in electronics and electrical communication engineering with a specialization in VLSI from IIT Kharagpur (IIT KGP), Kharagpur, India, in 2018. He is currently pursuing the M.S. degree in Electrical and Computer Engineering at Georgia Institute of Technology, Atlanta, GA, USA. His research interests include bioelectronics and integrated sensor systems.

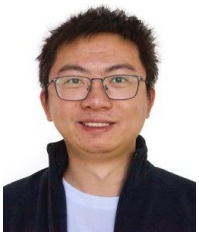

Jin Hao received the DMD degree and MS degree from Sichuan University, China. Jin's previous research interest was focused on disease modeling by 3D bioengineered methods. He received the Ph.D. degree in Biological Sciences in Dental Medicine at Harvard University, Cambridge MA, USA in 2022. Jin is investigating the role of TBK1 in neurodegenerative diseases, in particular, ALS. He is aiming to model ALS in CRISPR-edited hESCs and mouse models and trying to understand the mechanism of TBK1 mutation in ALS development.

Yu S. Zhang received the B.Eng. degree in Biomedical Engineering from Southeast University, China, in 2008, after which he then obtained the M.S. degree in Biomedical Engineering from Washington University in St. Louis, St. Louis, MO, USA, in 2011. He received the Ph.D. degree in Biomedical Engineering at Georgia Institute of Technology and Emory University School of Medicine, Atlanta, GA, USA, in 2013. Dr. Zhang is an Assistant Professor of Medicine at Harvard Medical School and Associate Bioengineer in the Division of Engineering in Medicine at the Brigham and Women's Hospital. Dr. Zhang's research is focused on innovating medical engineering technologies, including 3D bioprinting, organs-on-chips, microfluidics, and bioanalysis, to recreate functional tissues and their biomimetic models. He is an author of over 160 peer-reviewed publications with an h-index of 44. His scientific contributions have been recognized by over 40 international, national, and regional awards, notable ones including TERMIS-AM Young Investigator Award, C&EN Talented 12, IEEE Photonics Society Young Investigator Award, Society for Mechanical Engineers Marcus Crotts Outstanding Young Manufacturing Engineer Award, IEEE Sensors Council Technical Achievement Award, Lush Prize—Young Researcher (Americas), and Baxter Young Investigator Award.

Kevin Eggan received the B.S. degree in microbiology and immunology from the University of Illinois, Champaign, IL, USA, in 1996, and a Ph.D. in biology from MIT, Cambridge, MA, USA, in 2003, where he focused on cloning, stem cells and reprogramming after nuclear transfer under the guidance of genetics pioneer Rudolf Jaenisch, Ph.D. Dr. Eggan served as a tenured Professor in the Department of Stem Cell and Regenerative Biology at Harvard University, Director of Stem Cell Biology for the Stanley Center for Psychiatric Research at the Broad Institute, and an Institute Member of the Broad Institute of Massachusetts Institute of Technology (MIT) and Harvard. Dr. Eggan has published over 130 scientific articles and holds 13 patents. He received the MacArthur Foundation's "Genius Grant" and was named one of 50 Howard Hughes Medical Institute Early Career Scientists, among other distinctions. In addition, Dr. Eggan has served on the Scientific Advisory Boards of Ipierian, Roche, and Angelini Pharma.

Hua Wang (Senior Member, IEEE) is an associate professor at the School of Electrical and Computer Engineering (ECE) at Georgia Institute of Technology and the director of Georgia Tech Electronics and Micro-System (GEMS) lab. Prior to that, he worked at Intel Corporation and Skyworks Solutions on mm-Wave integrated circuits and RF front-end modules. He received his M.S. and Ph.D. degrees in electrical engineering from the California Institute of Technology, Pasadena, in 2007 and 2009, respectively. Dr. Wang is interested in innovating analog, mixed-signal, RF, and mm-Wave integrated circuits and hybrid systems for wireless communication, sensing, and bioelectronics applications. He has authored or co-authored over 170 peer-reviewed journal and conference papers. Dr. Wang received the DARPA Director's Fellowship Award in 2020, the DARPA Young Faculty Award in 2018, the National Science Foundation CAREER Award in 2015, the Qualcomm Faculty Award 2020, the IEEE MTT-S Outstanding Young Engineer Award in 2017, the Georgia Tech Sigma Xi Young Faculty Award in 2016, the Georgia Tech ECE Outstanding Junior Faculty Member Award in 2015, and the Lockheed Dean's Excellence in Teaching Award in 2015. He held the Demetrius T. Paris Professorship from 2014 to 2018. His GEMS research group has won multiple academic awards and best paper awards, including the 2019 Marconi Society Paul Baran Young Scholar, the IEEE RFIC Best Student Paper Awards (1st Place in 2014, 2nd Place in 2016, and 2nd Place in 2018), the IEEE CICC Outstanding Student Paper Awards (2015, 2018, and 2019), the IEEE CICC Best Conference Paper Award (2017), the 2016 IEEE Microwave Magazine Best Paper Award, and the IEEE SENSORS Best Live Demo Award (2nd Place in 2016). Dr. Wang is a Technical Program Committee (TPC) Member for IEEE ISSCC, RFIC, CICC, and BCICTS conferences. He is a Steering Committee Member for IEEE RFIC and CICC. He is the Conference Chair for CICC 2019 and Conference General Chair for CICC 2020. He is a Distinguished Lecturer (DL) for the IEEE Solid-State Circuits Society (SSCS) for the term of 2018-2019. He serves as the Chair of the Atlanta's IEEE CAS/SSCS joint chapter that won the IEEE SSCS Outstanding Chapter Award in 2014